Scaling K2. VI. Reduced Small-planet Occurrence in High-galactic-amplitude Stars

Jon K. Zink[1,17] , Kevin K. Hardegree-Ullman[2] , Jessie L. Christiansen[3] , Erik A. Petigura[4] , Kiersten M. Boley[5,18] ,
Sakhee Bhure[3,19] , Malena Rice[6,7,20] , Samuel W. Yee[8] , Howard Isaacson[9,10] , Rachel B. Fernandes[11,12] ,
Andrew W. Howard[13] , Sarah Blunt[13] , Jack Lubin[14] , Ashley Chontos[15,21] , Daria Pidhorodetska[16] , and
Mason G. MacDougall[4]
[1] Department of Astronomy, California Institute of Technology, Pasadena, CA 91125, USA; jzink@astro.caltech.edu
[2] Steward Observatory, The University of Arizona, Tucson, AZ 85721, USA
[3] Caltech/IPAC-NASA Exoplanet Science Institute, Pasadena, CA 91125, USA
[4] Department of Physics and Astronomy, University of California, Los Angeles, CA 90095, USA
[5] Department of Astronomy, The Ohio State University, Columbus, OH 43210, USA
[6] Department of Physics and Kavli Institute for Astrophysics and Space Research, Massachusetts Institute of Technology, Cambridge, MA 02139, USA
[7] Department of Astronomy, Yale University, New Haven, CT 06511, USA
[8] Department of Astrophysical Sciences, Princeton University, 4 Ivy Lane, Princeton, NJ 08544, USA
[9] 501 Campbell Hall, University of California at Berkeley, Berkeley, CA 94720, USA
[10] Centre for Astrophysics, University of Southern Queensland, Toowoomba, QLD, Australia
[11] Lunar and Planetary Laboratory, The University of Arizona, Tucson, AZ 85721, USA
[12] Alien Earths Team, NASA Nexus for Exoplanet System Science, USA
[13] Department of Astronomy, California Institute of Technology, Pasadena, CA 91125, USA
[14] Department of Physics & Astronomy, University of California Irvine, Irvine, CA 92697, USA
[15] Department of Astrophysical Sciences, Princeton University, 4 Ivy Lane, Princeton, NJ 08540, USA
[16] Department of Earth and Planetary Sciences, University of California, Riverside, CA, USA

Abstract

In this study, we performed a homogeneous analysis of the planets around FGK dwarf stars observed by the Kepler and K2 missions, providing spectroscopic parameters for 310 K2 targets —including 239 Scaling K2 hosts—observed with Keck/HIRES. For orbital periods less than 40 days, we found that the distribution of planets as a function of orbital period, stellar effective temperature, and metallicity was consistent between K2 and Kepler, reflecting consistent planet formation efficiency across numerous ~1 kpc sight-lines in the local Milky Way. Additionally, we detected a $3\times$ excess of sub-Saturns relative to warm Jupiters beyond 10 days, suggesting a closer association between sub-Saturn and sub-Neptune formation than between sub-Saturn and Jovian formation. Performing a joint analysis of Kepler and K2 demographics, we observed diminishing super-Earth, sub-Neptune, and sub-Saturn populations at higher stellar effective temperatures, implying an inverse relationship between formation and disk mass. In contrast, no apparent host-star spectral-type dependence was identified for our population of Jupiters, which indicates gas-giant formation saturates within the FGK mass regimes. We present support for stellar metallicity trends reported by previous Kepler analyses. Using Gaia DR3 proper motion and radial velocity measurements, we discovered a galactic location trend; stars that make large vertical excursions from the plane of the Milky Way host fewer super-Earths and sub-Neptunes. While oscillation amplitude is associated with metallicity, metallicity alone cannot explain the observed trend, demonstrating that galactic influences are imprinted on the planet population. Overall, our results provide new insights into the distribution of planets around FGK dwarf stars and the factors that influence their formation and evolution.

1. Introduction

The Kepler Space Telescope identified over 4700 transiting exoplanet candidates (NASA Exoplanet Archive 2023) through continuous photometric monitoring of a single patch of the sky (Koch et al. 2010; Borucki et al. 2011). This field was selected

because of the predominance of Sun-like stars, in hopes that these stars would yield a meaningful occurrence rate for Earth analogs (Batalha et al. 2010). The consistency of the mission photometry enabled the development of automated search algorithms (Jenkins et al. 2010) and accurate quantification of the sample biases (Petigura et al. 2013b; Christiansen et al. 2015; Dressing & Charbonneau 2015; Christiansen 2017; Coughlin 2017; Christiansen et al. 2020). Early work found that the small-planet populations ($<4R_\oplus$) follow a power law in both radius and period space (Youdin 2011; Howard et al. 2012; Dressing & Charbonneau 2013; Petigura et al. 2013a; Dressing & Charbonneau 2015; Muirhead et al. 2015), suggesting an abundant population of small short-period planets with no solar system equivalent. The final processing of DR25 (Thompson et al. 2018) has been used ubiquitously throughout the field to understand the underlying occurrence of

exoplanets in our local region of the galaxy. Numerous first-order results have transpired from Kepler DR25, including high-confidence occurrence estimates for the super-Earths, sub-Neptunes, sub-Saturns, and Jupiters within 100 day periods (e.g., Mulders et al. 2018; Petigura et al. 2018a; Hardegree-Ullman et al. 2019; He et al. 2019; Hsu et al. 2019; Zink et al. 2019a). These strong results provide an excellent estimate for the local galactic exoplanet population, but the biases imposed by the original field selection have yet to be fully explored.

After the spacecraft underwent an operational malfunction, the telescope could no longer remain pointed at the Kepler field. Thoughtful field selection along the ecliptic plane reduced the ongoing solar pressure that caused persistent spacecraft drift, providing an opportunity to probe unique stellar populations and test the robustness of the Kepler results. The K2 mission was born out of this spacecraft pointing issue and 19 unique fields were observed, representing a more isotropic sampling of the local galaxy (Howell et al. 2014; Van Cleve et al. 2016). Unfortunately, the reaction-wheel malfunction that concluded the primary Kepler mission riddled the K2 photometry with correlated noise variations, which could not be addressed with the base Kepler software. This led to numerous community-based efforts to systematically remove these spacecraft artifacts and identify new planet signals (Luger et al. 2016; Vanderburg et al. 2016; Luger et al. 2018; Petigura et al. 2018). Eventually, nearly 1000 new planets would be identified in K2 photometry through piecemeal efforts (Barros et al. 2016; Adams et al. 2016; Crossfield et al. 2016; Pope et al. 2016; Dressing et al. 2017; Livingston et al. 2018; Mayo et al. 2018; Yu et al. 2018; Kruse et al. 2019; Zink et al. 2019b). However, the absence of a rigorous homogeneous analysis of the photometry made it difficult to carry out robust demographic analyses.

The Scaling K2 series provided the first homogeneously derived stellar (Hardegree-Ullman et al. 2020) and planet (Zink et al. 2020a, 2021) samples and the catalog measurements needed to perform robust occurrence rates using the K2 planet sample. We provide further discussion of these samples and the filters used to focus our current study and ensure purity in Sections 2 and 3 of this paper. In Scaling K2 III, we provided early planet occurrence results from our catalog (using only the Campaign 5 sample), showing our pilot study had consistent occurrence measurements with Kepler (Zink et al. 2020b). In Scaling K2 V, we validated 60 new planet detections (Christiansen et al. 2022), providing further evidence that our novel planet detections were robust against astrophysical false positives. In this work, we used the full catalog to provide robust planet occurrence results, as dictated by our forward-modeling technique described in Section 4, for the entirety of the transit-based K2 campaigns, and we compared these results with an analogous Kepler demographic analysis in Section 5. We also tested established stellar trends and identified a new location-based parameter in Section 6. We discuss our findings in Section 7 and conclude with a summary of our findings in Section 8.

2. The Stellar Sample

The focus of this work is to compare planet occurrence between the Kepler and K2 missions. We chose to limit our study to FGK stars, which were well sampled by the K2 and Kepler target selection functions. The analysis of incomplete exoplanet samples, as done here, requires a strong grasp of the

underlying stellar population the respective planets have been drawn from. For this study we begin with the Berger et al. (2020b) catalog for Kepler stars and the Hardegree-Ullman et al. (2020) catalog for the K2 stellar sample. We acknowledge that these two studies used unique methodologies for deriving stellar parameters; Berger et al. (2020b) used photometric mapping to isochrone models, while Hardegree-Ullman et al. (2020) relied on empirically based parameters photometrically optimized through a random forest classifier. The different methodologies may lead to systematic offsets, but Zink et al. (2020b) tested these two catalogs against the homogeneously derived Gaia DR2 stellar radius[22] parameters and found an average offset of $0.06 R_\odot$ between these two catalogs, which is comparable to the 5% uncertainty exhibited by a majority of individual stellar radius measurements.

In an effort to reduce parameter uncertainties, we updated the [Fe/H], $\log g$, and $T_{\rm eff}$ values to reflect the most recent spectroscopic surveys, including LAMOST DR8 (Wang et al. 2022), APOGEE DR17 (Abdurro'uf et al. 2022), the CKS survey (Petigura et al. 2017a), 73 existing Keck/HIRES K2 target parameterizations (Petigura et al. 2018), and 237 new K2 target characterizations using Keck/HIRES.[23] These new target spectra follow the CKS survey-processing protocol and provide the same level of homogeneity and precision; see Appendix A for a detailed account of our new stellar parameters. In testing we found a vast majority of the spectra-based updates are within the previously determined measurement uncertainties, minimizing any systematic changes. In particular, both LAMOST and APOGEE [Fe/H] values exhibited an average 0.02 dex offset when compared to overlapping targets in the CKS catalog, well within the reported 0.03–0.1 dex uncertainty of either of these surveys. Further discussion of these precise parameter values can be found in Section 6.

We began with the entirety of both catalogs, comprising 186,301 Kepler targets and 222,088 unique K2 targets. We isolated the FGK stars by selecting targets with $T_{\rm eff}$ between 4000 and 6500 K, removing 19,697 Kepler and 52,727 K2 targets. To ensure these targets were dwarfs, we follow the advisement of Huber et al. (2016) and only selected stars with

$$\log g \geqslant \frac{\arctan\left(\frac{6300K - T_{\rm eff}}{67.172K}\right)}{4.671} + 3.876 \text{ dex}, \qquad (1)$$

excluding 61,056 Kepler stars and 73,963 K2 stars. The $4''$ pixel width of the spacecraft instrument allows for unresolved stellar companions. We relied on the Gaia Renormalized Unit Weight Error (RUWE) metric to minimize this potential source of contamination and only included targets with RUWE <1.4 (as suggested by Lindegren et al. 2018). Additionally, Gaia DR3 provides a flag, "non_single_star," which denotes sources that provide evidence of a binary. Removing targets with Gaia binary

---

[22] Stellar radius measurements have the greatest impact on occurrence measurements because of the sample detection efficiency's strong dependence on the projected stellar area. Systematic effects from other parameterization differences will be minor and are unlikely to produce significant occurrence offsets between the samples.
[23] Existing homogeneous stellar characterization using Gaia DR3 from Creevey et al. (2022), Fouesneau et al. (2022), Andrae et al. (2022), and Berger et al. (2023) relied on the spacecraft's low-resolution Bp/Rp spectrograph. The constraining power of this instrument appears to be on order of 0.2 dex for [Fe/H] in its current form and requires careful offset correction; see Figure 1 of Berger et al. (2023). To avoid sample contamination, we did not include these parameter updates in our stellar sample.
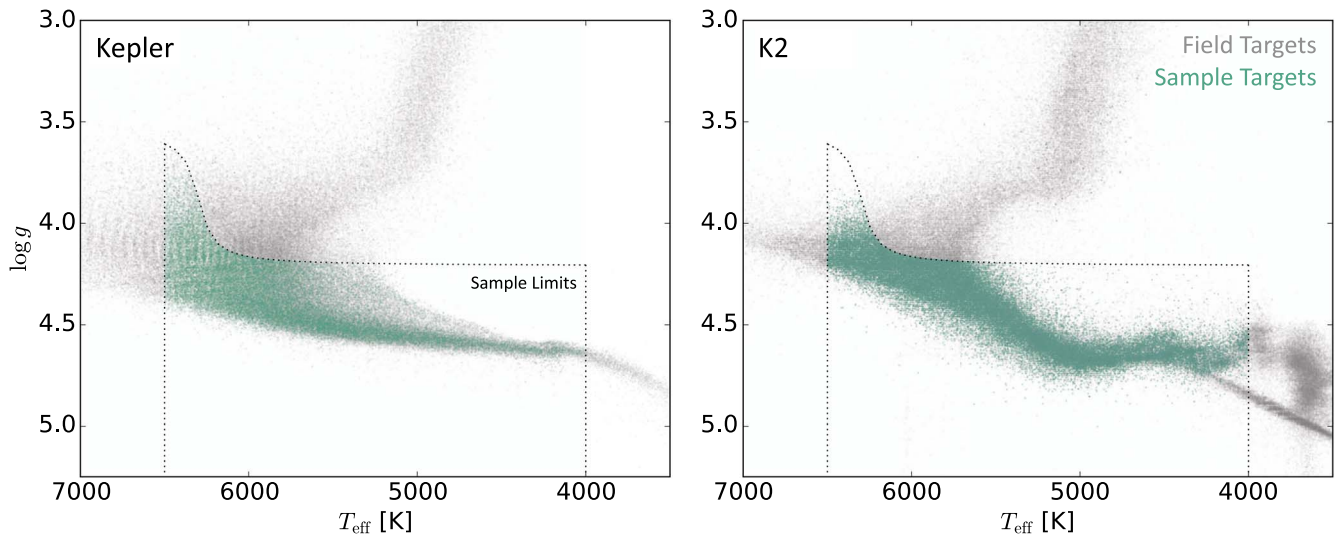
Figure 1. The stellar sample from Kepler and K2 portrayed in the $T_{\rm eff}$ and $\log g$ plane. The gray points show the Kepler and K2 field sample, while the colored dots highlight the FGK dwarfs selected for this study.
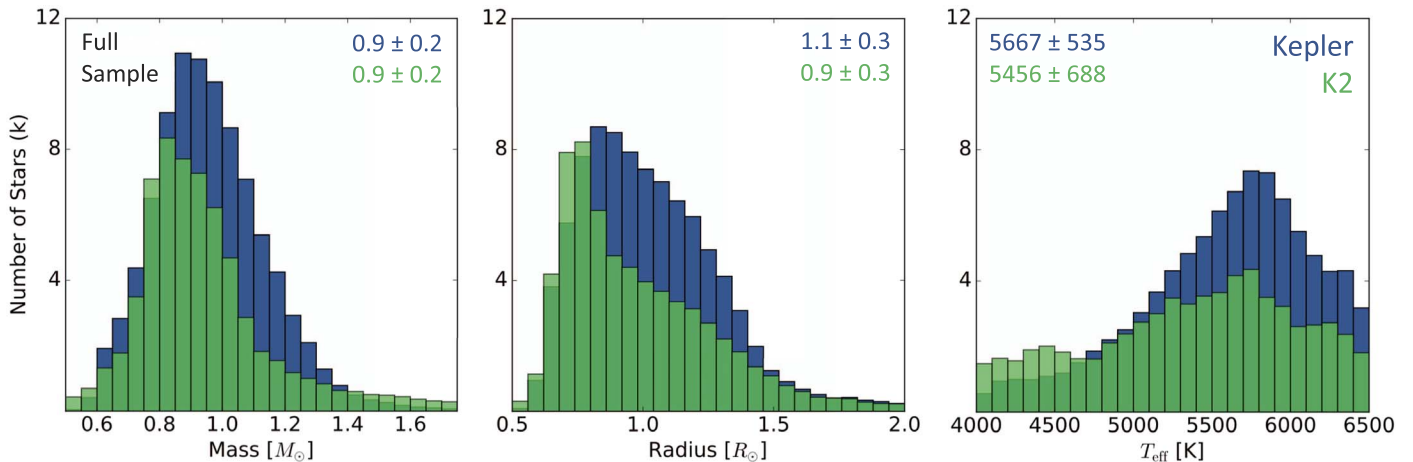
Figure 2. A comparative display of the Kepler and K2 FGK stellar parameters. The y-axis shows the number of stars in each bin in units of 1000 stars. The median and median absolute deviation values for each distribution are reported in the upper corner of each plot. We provide the stellar mass for a population-level visual comparison, noting the dominance of a loose photometric constraint within our sample.

flags and high RUWE values, we excluded 14,410 Kepler and 31,017 K2 targets. The remaining sample may consist of photometrically turbulent targets, which will not yield meaningful candidates and only slow down the occurrence processing. Therefore, we placed an upper bound on the photometric noise metric known as the combined differential photometric precision (CDPP; Christiansen et al. 2012). For Kepler we required $\rm CDPP_{7.5hr} < 1000$ ppm, excluding 288 targets, and $\rm CDPP_{8hr} < 1200$ ppm for K2 excluding an additional 11,425 targets. We found 90,850 Kepler and 64,454 K2 stars met the discussed criteria and labeled this selection of stars as our Full Sample (in Section 6, we limit this sample further). The selected catalog of stars is displayed in Figure 1 against the background of the total field sample.

2.1. Kepler and K2 Sample Comparison

The cuts selected for FGK dwarfs; however, the exact distribution of FGK dwarfs is slightly different between the two missions. In Figure 2 we show the relevant stellar parameter distributions for both Kepler and K2. Overall, there is a

general consistency between both sets of stars. Under more careful inspection, it appears the K2 sample is on average $\sim$200 K cooler and $\sim$0.2$R_\oplus$ smaller than the Kepler stellar sample. We provide a detailed discussion of the dependence of spectral class on planet occurrence in Section 6.

3. The Planet Sample

We drew our sample of planets from the two available homogeneous catalogs, Kepler DR25 (Thompson et al. 2018) with updates from Berger et al. (2020a) and Scaling K2 (Zink et al. 2021). Both catalogs provide the necessary completeness measurements needed to carry out a robust statistical analysis. Before slicing this sample into the required bins, it is worth considering the potential for systematic offsets between the catalog parameters. The three-transit minimum requirement of each catalog reduces period uncertainties to within 0.01%, rendering any existing offsets negligible. However, the planet radii are subject to significant modification from the necessary data-processing schemes, requiring a more detailed examination. Christiansen et al. (2015) considered how the Kepler PDC pipeline impacted the radius parameters by looking for offsets

between the injected (known values) and recovered (measured values) planet signals. Overall, the software systematically reduced the planet radius by 1.7%, well within the 5% uncertainty presented in each catalog. The K2 light curves required even further processing, given the consistent drift of the telescope. Zink et al. (2020a) considered how this additional detrending would impact the measured radius values through an analogous comparison of the injected and recovered signals, finding a 2.3% average reduction in radius parameters. Again, this offset is well within the expected uncertainty. Furthermore, these two radius reduction estimates are in the same direction. Thus, the systematic radius offset between these catalogs is only ∼0.6%, which is negligible and will not impact our overall analysis and comparisons.

We started with the complete Kepler DR25 planet candidate sample (4612 candidates). We then removed 1647 candidates not hosted by stars in our stellar sample. It is important that our samples span comparable period ranges, so we excluded candidates with periods less than 1 day (101 candidates) and periods beyond 40 days (667 candidates). To ensure purity and minimize the contamination from eclipsing binaries, we required an impact parameter of $b < 0.9$, removing 236 planets from our sample. We limit the sample to planet radii to within 1–$20R_{\oplus}$ (excluding 243 additional candidates). Brown dwarfs exist within this radius range, but secondary eclipse analyses within the Kepler and K2 automated software remove many of these emitting candidates. Furthermore, short-period brown dwarf occurrence is less than $6\times$ that of giant planets (Csizmadia et al. 2015), rendering any remaining contamination negligible. After these cuts, we were left with 1718 Kepler planet candidates. Making equivalent cuts in the Scaling K2 planet catalog, we retain 320 K2 planets.

The two planet samples are displayed in Figure 3. The population of super-Earths and sub-Neptunes, spanning 1–$4R_{\oplus}$, appears divided by a dearth of planets near $2R_{\oplus}$, known colloquially as the radius valley (Fulton et al. 2017). This sparsely populated region of parameter space highlights an evolutionary process, where planets with thick H/He atmospheres and low surface gravity undergo mass loss (e.g., photoevaporation: Owen & Wu 2017; core-powered mass loss: Gupta & Schlichting 2019), removing much of this thick atmosphere. These stellar proximity dependent mechanisms separate the sub-Neptunes from the super-Earths. We chose to use a physically motivated bound for these planet classes and employed the empirically derived radius valley period function in Ho & Van Eylen (2023)[24] as our divider. The separation between the other classes of planets is less clear; thus, we used 4–$8R_{\oplus}$ for sub-Saturns and 8–$20R_{\oplus}$ for Jupiters.

4. Forward Modeling with ExoMult

The aim of this paper is to compare Kepler and K2 planets—when possible—and to expand the stellar host parameter space of the Kepler planet sample to refine existing trends. In order to make these two planet catalogs compatible, it is essential to properly account for each sample's unique completeness features. To do so, we implemented our forward-modeling software

---

[24] We used the two-dimensional support-vector machine model from Ho & Van Eylen (2023), which was derived using the Kepler sample alone. Thus, we assumed the valley would be consistent within the K2 sample, as shown by Hardegree-Ullman et al. (2020). However, we acknowledge that differences may arise from dissimilarities in the underlying stellar-mass populations but expect these variations to be minimal.

ExoMult (Zink et al. 2019a, 2020b), which simulates the population of observed planets given some initial parent distribution. Forward modeling provides a straightforward method of accounting for catalog differences and sample reliability. This software package draws planets from around a sample of Kepler and K2 stars, subjected each simulated planetary system to the geometric and instrumental selection criterion for each corresponding mission. Within ExoMult, we used the Hsu et al. (2019) and Zink et al. (2021) completeness functions to respectively account for Kepler and K2 detection/vetting biases. To simplify our calculation, we did not attempt to match the cataloged system multiplicities, treating each planet as an independent detection. If multiplicity was required to reproduce the Kepler and K2 observed planet total, we drew all multiplanet systems from a perfectly aligned disk (i.e., no mutual inclination). We also assumed all planets have zero eccentricity, which is motivated by the low-eccentricity population distributions found for these short-period planets that are sensitive to tidal circularization (e.g., Shabram et al. 2016). Some warm giants considered in this study have heightened eccentricities, but our assumption can be made without loss of generality due to competing completeness effects. High-eccentricity transits on average project a shorter transit duration and orbit closer to the host star, reducing the signal strength while increasing the transit probability. Miraculously, these effects nearly cancel out (Burke 2008), with some minor complications in multiplanet systems (see Section 8.5 of Zink et al. 2019a).

4.1. Model

The simulated planets in this study were initially drawn from a broken power law $g(P)$ in orbital period space and a single power law $q(R)$ in planet radius space as has been done in numerous other exoplanet occurrence studies (e.g., Youdin 2011; Petigura et al. 2013a; Mulders et al. 2018; Zink et al. 2019a):

$$g(P) \propto \begin{cases} P^{\beta_1} & \text{if } P < P_{br} \\ P^{\beta_2} & \text{if } P \geqslant P_{br} \end{cases}$$
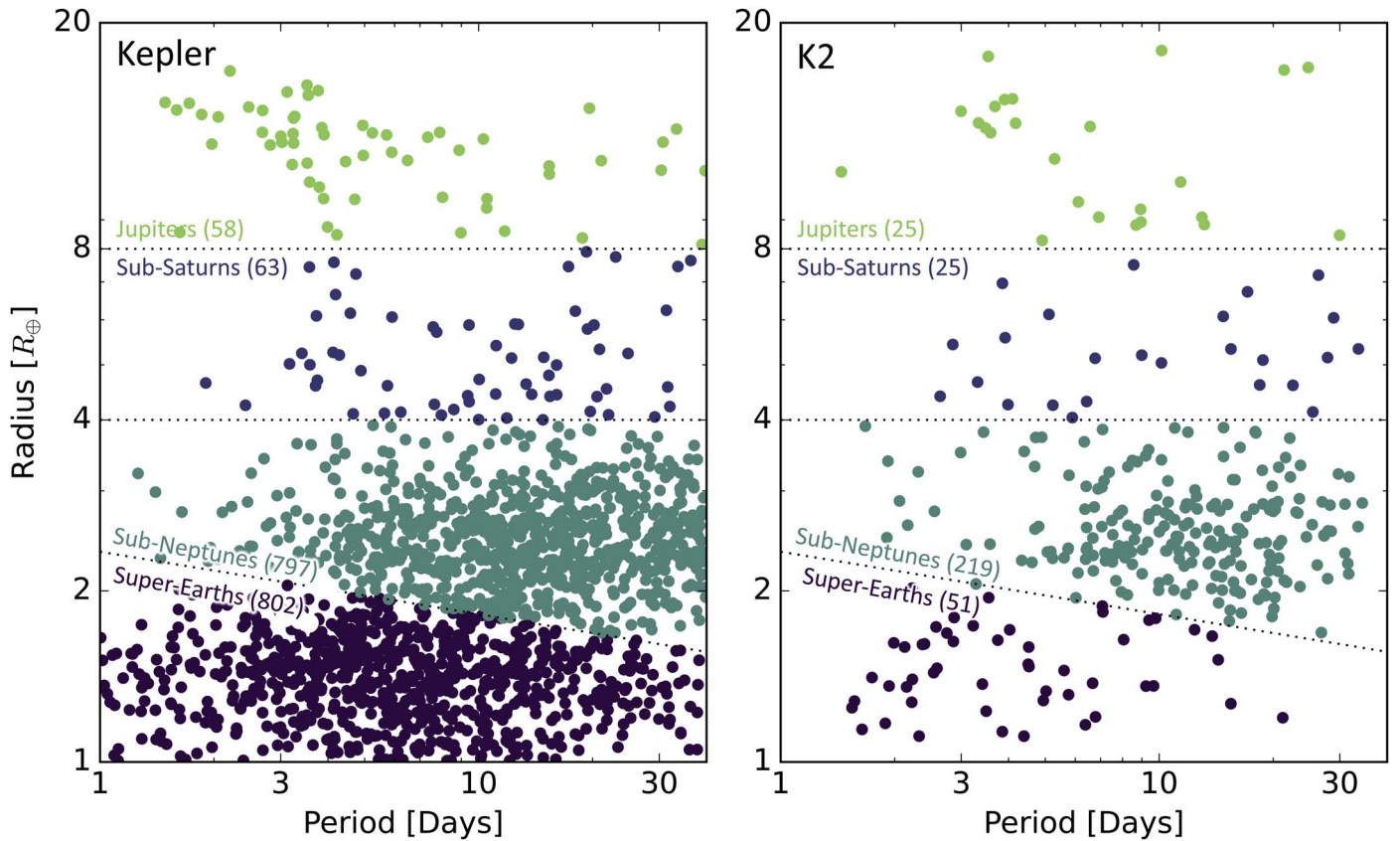$$q(R) \propto R^{\alpha}, \qquad (2)$$

where P_{br} represents the corresponding break in the period power law and the β values are the scaling model parameters. Inherent in this model is the assumption of radius and period independence. Several studies (e.g., Fulton et al. 2017; Van Eylen et al. 2018) have identified a population valley that separates the super-Earths from the sub-Neptunes, indicating the existence of covariance between these parameters. By partitioning the planet sample along this valley, we minimize such complications. Our occurrence model n was then normalized by a factor f, which represents the number of planets per star within the range of our sample:

$$\frac{d^2 n}{d \log P \, d \log R} = f \, g(P) \, q(R). \qquad (3)$$

4.2. Optimization

To optimize this forward-modeling procedure against our observed planet samples, we relied on the methodology presented in Zink et al. (2020b). In brief, the cumulative distribution function (CDF) for the simulated population was compared to the observed population for each relevant

Figure 3. The sample of Kepler and K2 planets selected for this demographic analysis. The gray dotted line separates the planet classes accordingly. The number of planets in each bin is denoted next to the respective class title. We employed the two-dimensional support-vector machine model from Ho & Van Eylen (2023) for our super-Earth/sub-Neptune bound.

parameter. The Anderson–Darling test statistic, which provides an exponential scaling with the likelihood function, was used to identify more favorable models. This procedure is effective in replicating the shape of the underlying population, but CDFs are sample size independent, providing no constraint on the total number of planets. To constrain the number of planets expected, we relied on a modified Poisson likelihood function (see Equation (3) of Zink et al. 2020b), which provides a probabilistic comparison of the normalization of two drawn populations.

The posterior distribution for each corresponding parameter was measured using a Bayesian framework. We assumed uniform priors for all corresponding parameters with physically motivated bounds (i.e., we did not allow for negative occurrence fractions). Overall, we found that all imposed bounds exceeded the 10σ range of any identified model parameters, indicating the posteriors were not impacted by these boundary choices. To measure the posteriors for each parameter, we used the `emcee` affine-invariant MCMC algorithm (Foreman-Mackey et al. 2014).

5. Results

Here we focus on how the Kepler planet occurrence rates compare with the K2 rates for the four relevant planet classes.

5.1. Super-Earths

For the super-Earths, we found increasing planet occurrence from 1 to 6 days for both Kepler ($\beta_1 = 1.9 \pm 0.3$) and K2 ($\beta_1 = 1.7 \pm 0.4$), which is shallower than numerous other

occurrence calculations (e.g., Petigura et al. 2018a found $\beta_1 = 2.4 \pm_{0.3}^{0.4}$). Previous studies have used a constant radius upper limit (usually around 2 $R_\oplus$); however, we chose a functional form that follows the physical limits associated with the radius valley (Fulton et al. 2017). This flattening of short-period occurrence is due to our empirically motivated assignment of super-Earth classification for a wider range of radii at short periods. Work by Bergsten et al. (2022), who also used a nonfixed upper radius limit, found a comparable $1.44 < \beta_1 < 2.90$ for this stellar-mass range. This occurrence reduction within 6 days may be indicative of the inner edge of the gas disk (Mullally et al. 2015) having been truncated by the host star's magnetosphere (Lee & Chiang 2017), producing a distinct pile-up location at which planets may have an enhanced formation rate (Boley et al. 2014) or may be preferentially trapped in the process of migration (Baillié et al. 2016). Our noted reduction in β_1, from previous studies, indicates that super-Earth formation has a weak period dependence near the host star.

Around 6 days, planet occurrence turns over (Kepler: $P_{br} = 5.9 \pm 1.3$ days; K2: $P_{br} = 8.9 \pm_{6.24}^{7.4}$ days). Both Kepler and K2 P_{br} values are statistically consistent with the 7–10 day value found by previous studies (Youdin 2011; Howard et al. 2012; Burke et al. 2015; Petigura et al. 2018a). However, a reduction in our Kepler model—which drew from the same planet sample as the previous works— suggests a more nuanced interpretation. Furthermore, our combined model, which performed a joint analysis of Kepler and K2 populations, produced an even closer-in population peak ($P_{br} = 5.6 \pm 1.1$ days). The root

Table 1
The Model Parameters for Our Optimization of Kepler and K2 Planet Occurrence

Class	Mission	f	α	β_1	P_{br}	β_2
SE						
	Kepler	0.31 ± 0.02	-1.0 ± 0.2	1.9 ± 0.3	5.9 ± 1.2	0.2 ± 0.2
	K2	0.48 ± 0.21	-1.9 ± 0.7	1.7 ± 0.4	$8.9^{7.4}_{6.24}$	0.5 ± 1.2
	Combined	0.31 ± 0.02	-1.1 ± 0.2	2.0 ± 0.2	5.6 ± 1.1	0.2 ± 0.2
SN						
	Kepler	0.28 ± 0.01	-1.5 ± 0.1	2.6 ± 0.5	8.5 ± 2.4	0.6 ± 0.2
	K2	0.59 ± 0.10	-2.0 ± 0.3	2.8 ± 0.6	$10.9^{5.0}_{3.9}$	0.9 ± 0.7
	Combined	0.30 ± 0.01	-1.7 ± 0.1	2.5 ± 0.4	9.5 ± 2.0	0.5 ± 0.2
SS						
	Combined	0.019 ± 0.002	-2.7 ± 0.6	1.7 ± 0.5	$8.7^{7.8}_{4.8}$	0.5 ± 0.5
J						
	Combined	0.011 ± 0.002	-0.9 ± 0.4	2.7 ± 1.7	$3.4^{1.9}_{0.8}$	-0.1 ± 0.3

Note. The models are separated into planet classes: super-Earths (SE), sub-Neptunes (SN), sub-Saturns (SS), and Jupiters (J).

of the break reduction can again be traced to our upper limit for super-Earth classification. Bergsten et al. (2022), who also used a nonfixed upper radius limit, found a turnover period more in alignment with our values ($6 < P_{br} < 12$ days) for a comparable mass range, using the Kepler sample alone.

If planet cores were uniformly distributed in log-period space, P_{br} is expected to shift with stellar mass or insolation flux, providing hints of the underlying mass-loss mechanism. Petigura et al. (2022) were unable to discern a clear trend in P_{br} using a fixed $1.7 R_\oplus$ boundary, partially attributing this obfuscation to a nonuniform core distribution. However, our flattening population model suggests a more uniform primordial core-period distribution, suggesting trends with P_{br} may remain informative with careful planet classification. We leave further analysis of this trend with both Kepler and K2 for future studies. Regardless, it is clear that any negatively sloped functional radius bound will reduce P_{br} by capturing more short-period planets and reducing the number of longer-period planets considered super-Earths, as noted in Lopez & Rice (2018).

For Kepler, we found $\beta_2 = 0.2 \pm 0.2$, which is consistent with many previous studies (e.g., Petigura et al. 2018a: $\beta_2 = -0.3 \pm 0.2$). This trend remains flat even with our choice of a functional radius upper limit. The removal of contaminating long-period sub-Neptunes from our super-Earth sample provides a minor correction. Bergsten et al. (2022) found a range of values ($-0.1 < \beta_2 < 0.3$) using a nonconstant radius limit, aligning with our Kepler model parameters. Our K2 model is poorly constrained for the longer-period super-Earths ($\beta_2 = -0.5 \pm 1.2$). Only five K2 planets in our sample exist beyond 10 days. Overall, the K2 occurrence model is within 1σ of our Kepler model at all periods, suggesting consistent planet abundances.

To provide a more refined population model for super-Earths, we combine both Kepler and K2 samples and provide the optimized model parameters in Table 1. Overall, Kepler's abundant sample dominates the combined model fitting. However, the additional K2 planets allow us to provide a more precise occurrence model for the local galactic super-Earth population.
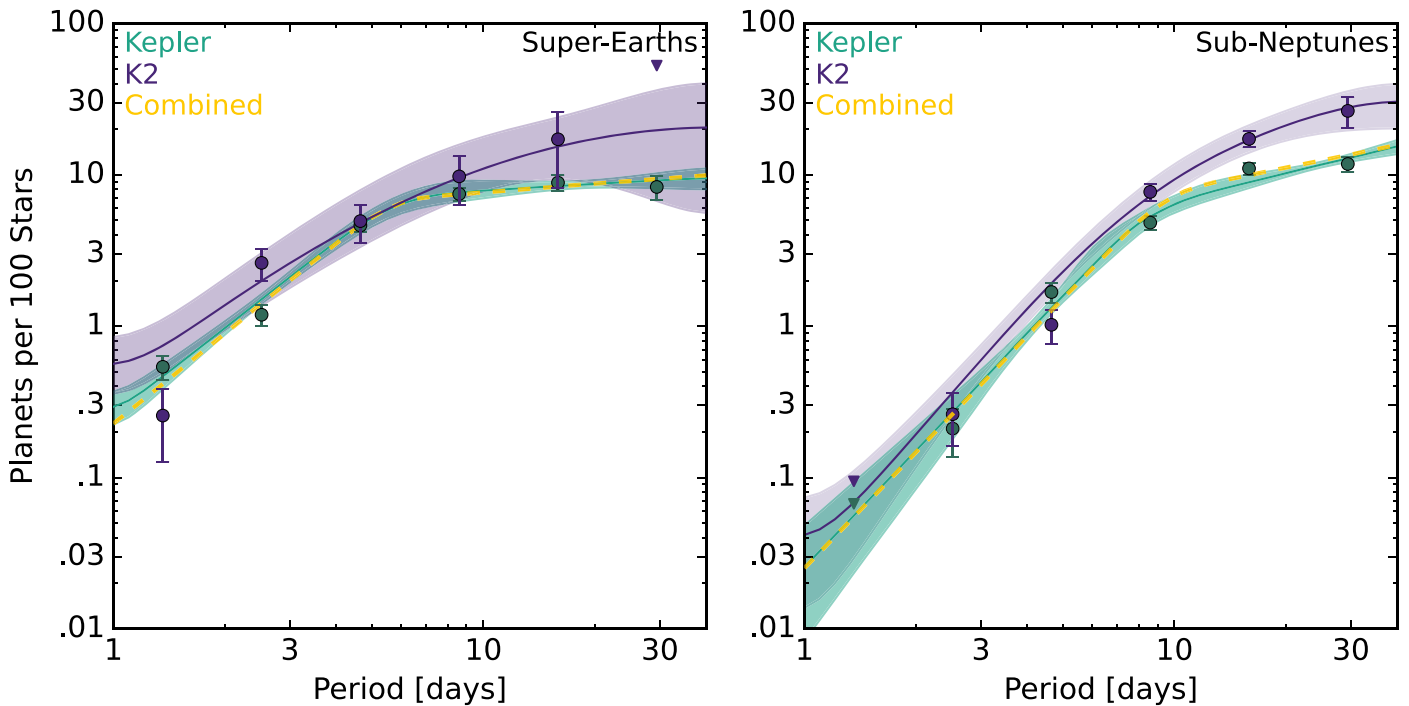
5.2. Sub-Neptunes

Sub-Neptunes have low densities due to their thick H/He atmospheres, which are susceptible to mass loss through either

early-stage integrated XUV flux photoevaporation (Owen & Wu 2017) or residual heat from within the planet's core (Gupta & Schlichting 2019). This transitional planet class is uniquely positioned to test and bound the formation processes responsible for gas giants and terrestrial planets. Our lower radius limits for sub-Neptunes are motivated by an observed dearth of planets expected from these mass-loss mechanisms.

Previous studies have found occurrences of around 30% for both sub-Neptunes and super-Earths orbiting FGK stars within 100 day periods (Youdin 2011; Howard et al. 2012; Burke et al. 2015), indicating an interconnected formation pathway. Since a vast majority of these planets orbit at shorter periods, our results confirm this consistency, finding $\sim$30% occurrence within 40 days for both populations. This population similarity may provide further evidence of a common origin for these two populations. We provide further discussion of this topic in Section 7.2.

An additional population deficit has been identified for sub-Neptunes with periods shorter than 10 days (Beaugé & Nesvorný 2013; Mazeh et al. 2016), where comparable period super-Earths are more abundant. This region of parameter space is well sampled within the Kepler mission catalog; thus, some physical process must be at play. The sub-Neptune desert likely reflects the saturation of photoevaporation or core-powered mass loss, removing the envelopes of nearly the entire planet-class radius range and generating an abundant population of short-period super-Earths with thin H/He atmospheres. Here, we found a consistent trend in both the Kepler ($\beta_1 = 2.5 \pm 0.5$) and K2 ($\beta_1 = 2.8 \pm 0.6$) sub-Neptune populations, which is in agreement with previous studies that used a constant radius bound (i.e., Petigura et al. 2018a: $\beta_1 = 2.3 \pm 0.2$). This consistency and minor trend enhancement is surprising. Naively, it might seem that a functional radius bound would produce a steeper trend by eliminating super-Earth contaminants, but Petigura et al. (2018a) used a more limited sample of hosts ($4700 < T_{eff} < 6500$ K). Since planetary mass-loss mechanisms have stellar-mass dependencies, it is likely our trend dictates a purer planet classification but is convolved with a wider range of stellar masses, blurring the overall short-period trend.

We observed a break in occurrence at $P_{br} = 8.5 \pm 2.4$ days for Kepler and $P_{br} = 10.9^{5.0}_{3.9}$ days for K2. These trends are within parameter uncertainty and agree with previous works (Youdin 2011; Howard et al. 2012; Burke et al. 2015), which

Figure 4. Our output occurrence models for the super-Earths and sub-Neptunes. The shaded regions illustrate the 1σ range for each respective model. Over the top of our optimized models, we provide binned occurrence values for reference. These binned values help guide the eye, but the fits were accomplished in the full unbinned data set. The triangle markers are 3σ upper bounds, representing sparsely populated regions of parameter space. The gold dotted line shows the best-fit combined Kepler and K2 model. The parameter values for these models are provided in Table 1.

found P_{br} around 10 days. Despite their statistical similarity, Figure 4 depicts an overall occurrence deviation between the Kepler and K2 sub-Neptune population near 10 days. Petigura et al. (2022) noted a similar normalization increase when comparing differences in host mass within the Kepler sample. Less-massive stars tend to harbor more sub-Neptunes while maintaining a comparable trend in period space. Our K2 stellar sample represents a slightly less-massive population when compared to the Kepler sample ($\Delta\tilde{M}_\star \sim -0.04 M_\odot$). This underlying stellar population difference likely explains the observed offset near 10 days. However, the K2 trend presented here does not provide a clear normalization offset and seems to enhance longer-period planets more. Petigura et al. (2018a) found a similar normalization trend, suggesting metal-rich stars harbor more sub 40 day sub-Neptunes. In Section 6.2 we show that K2 stars are generally metal poor compared to the Kepler population ($\Delta[\mathrm{Fe/H}] \sim -0.1$ dex), conflicting with the observed shift in K2 sub-Neptunes. The reality is likely a convolution of both stellar mass and [Fe/H].

Beyond 10 days, we observed a slight increase in planet occurrence (Kepler: $\beta_2 = 0.6 \pm 0.2$; K2: $\beta_2 = 0.9 \pm 0.7$). This deviates from previous work, which found an occurrence plateau (Petigura et al. 2018a; $\beta_2 \lesssim 0$). This surplus of long-period planets can again be attributed to our function class limit, accurately capturing more sub-Neptunes at longer periods.

Generally, we found consistency between the Kepler and K2 sub-Neptune samples, with a deviation for planets orbiting beyond 10 days. It is likely that these differences can be reconciled with careful accounting of the underlying stellar-mass distribution. This apparent cohesion supports the population and formation trends established by the Kepler planet catalog. For a more accurate occurrence model for the local galaxy, we provide a joint Kepler/K2 model in Table 1. The

super-Earths and sub-Neptunes population models have remarkable similarity, with a notable divergence in the period break, providing information on the underlying mechanisms imprinted on the planet population. We provide a detailed discussion of this difference in Section 7.1.

5.3. Sub-Saturns

Planet occurrence significantly drops for planets with $R > 4 R_\oplus$ (e.g., Fulton et al. 2017), indicating a unique formation pathway from that of the abundant sub-Neptune population. Empirically, these planets represent a population spanning 6–$60 M_\oplus$ with little planet radius correlation but a strong mass dependence on stellar [Fe/H] measurements (Petigura et al. 2017b). This suggests that metal-rich disks manifest more-massive sub-Saturn cores. Using interior-structure models (i.e., Lopez & Fortney 2013), several planets have been identified with core-mass fractions nearing 50% (e.g., K2-19 b: Petigura et al. 2020 and TOI-257 b: Addison et al. 2021). The prevalence of these heavy core sub-Saturns is at odds with the expectations of core-accretion planet formation (Pollack et al. 1996), which states that such massive cores should undergo runaway gas accretion and form Jovian-sized planets.

Previous measurements of occurrence have found nearly 7% of FGK stars host a sub-Saturn within 300 days (Petigura et al. 2018a). However, a majority of these planets lay at larger periods (>100 days). Adjusting existing results to the more limited 40 day period range of K2, they predict a $\sim$2% occurrence. Consistently, we found that $1.9\% \pm 0.2\%$ of FGK stars in the Kepler and K2 fields host sub-Saturns within 40 day periods (see Figure 5). The Jovian planets offer a remarkably comparable frequency ($1.1\% \pm 0.2\%$, see Section 5.4).
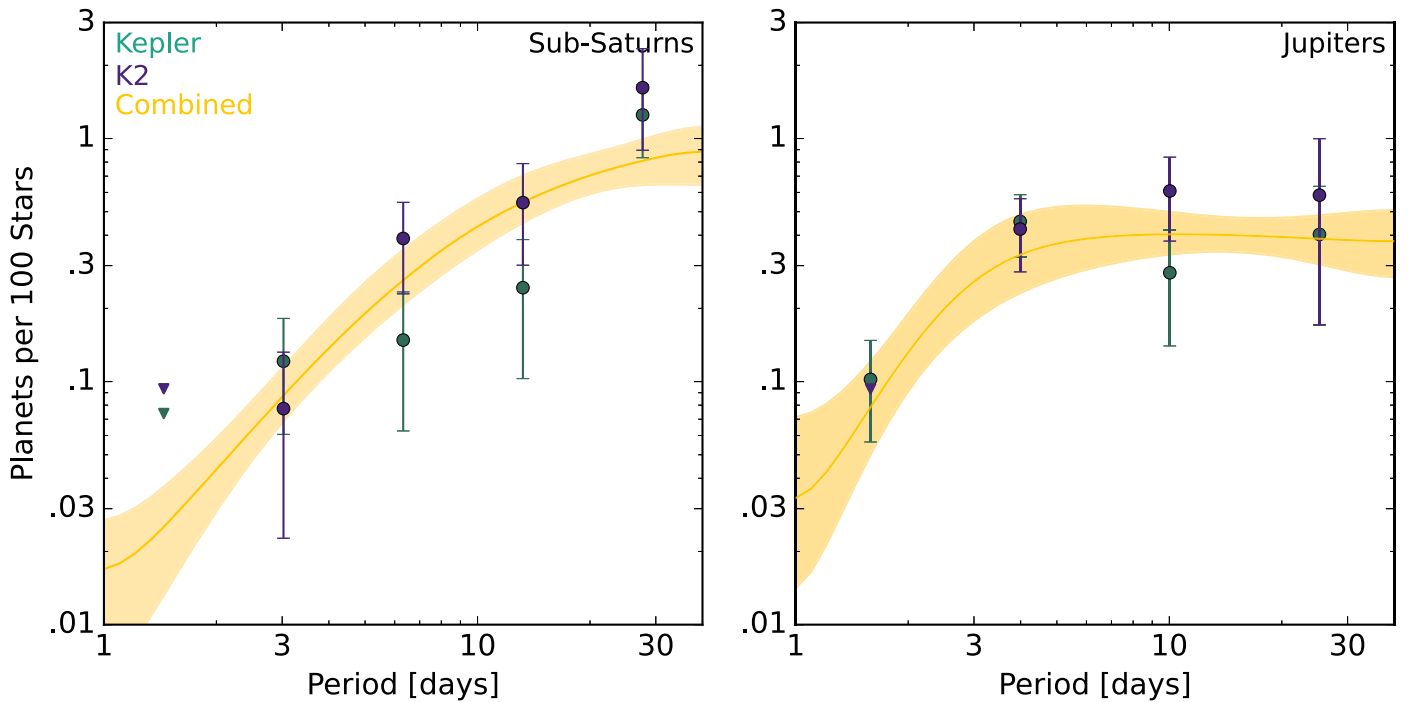
Figure 5. The same output occurrence models as those in Figure 4 but for the sub-Saturn and Jupiter populations. Independent modeling of the Kepler and K2 samples was not possible due to the limited number of detected planets in these classes. Thus, we provide a model and 1σ region for the joint population. The parameter values for these models are provided in Table 1.

Neither the Kepler nor K2 planet samples independently constrain our broken power-law model, but visual inspection of the occurrence values in Figure 5 shows consistency between Kepler and K2. Thus, we provide a joint analysis for a more robust population depiction. A steep decrease in occurrence is seen for planets with periods less than 10 days ($\beta_1 = 1.7 \pm 0.5$) matching previous results using the Kepler sample alone (Beaugé & Nesvorný 2013; Mazeh et al. 2016). Unlike the sub-Neptune population, these more-massive planets are not significantly impacted by early-stage photoevaporative mass loss (Ionov et al. 2018), requiring some additional mechanism like high-eccentricity migration in concert with tidal disruption (Owen & Lai 2018) to carve out the short-period region of parameter space. Alternatively, disk truncation may reduce in situ formation in this material-barren region of parameter space. Beyond the period break at $8.7^{+7.8}_{-4.8}$ days, sub-Saturn occurrence flattens ($\beta_2 = 0.5 \pm 0.5$). This significant population of warm sub-Saturns deviates from the Jovian population trend, suggesting a unique formation pathway. In Section 7.2.1 we provide further remarks on potential formation scenarios for sub-Saturns.

Overall, we found consistency with the Kepler and K2 samples for the sub-Saturn population and provide a refined population trend, lending credence to a complex formation pathway for gas giants.

5.4. Jupiters

The planets considered here are hot and warm Jupiters, which straddle the 10 day period marker. Their formation mechanisms are the subject of significant debate. Three major theories have been proposed to explain hot Jupiters, which seem to disobey standard core-accretion planet formation models. These gas giants may be born at a larger orbital radius and driven to a high-eccentricity orbit, where tidal forces

exhaust orbital angular momentum (high-eccentricity migration; Wu & Murray 2003; Fabrycky & Tremaine 2007; Nagasawa et al. 2008; Beaugé et al. 2012). Alternatively, these planets may have migrated inward through interactions with the disk itself (disk migration; Goldreich & Tremaine 1980; Lin et al. 1996). Tuned correctly, in situ formation may also be possible for these hot Jupiters (Batygin et al. 2016; Boley et al. 2016). Warm Jupiters, which span a range of 10–100 day periods, offer an origin further shrouded in mystery. Measurement of their host star's obliquity appears to favor orbital spin-axis alignment, suggesting warm Jupiters have a more quiescent formation history than their hot counterparts (Rice et al. 2022).

Like our sub-Saturn population, the Kepler and K2 samples are limited in their ability to independently constrain our model. Thus, we relied on a visual inspection of Figure 5 and observed occurrence consistency across missions. We provide a joint analysis for more robust population analysis. Hot- and warm-Jupiter occurrence rates appear to follow a broken power law, with the occurrence trend turning over around a three-day orbital period. The sharp decrease within three days ($\beta_1 = 2.7 \pm 1.7$) may be the outcome of tidal disruption events.

The three-day pile-up was first identified through early radial velocity (RV) surveys (e.g., Udry et al. 2003), which observed this peak in short-period giant occurrence. The emergence of the early Kepler sample brought into question the three-day pile-up, as transit demographic analyses failed to replicate the existing RV population feature (Howard et al. 2012; Fressin et al. 2013). Dawson & Murray-Clay (2013) later recovered a surplus of hot Jupiters at three days around the metal-rich Kepler stellar population, suggesting enhanced gas-giant production and a planet–planet scattering origin for some fraction of systems. Santerne et al. (2016) fully resolved a peak near five days in the Kepler sample with careful removal of

astrophysical false positives, reducing the tension with RV demographics. However, this two-day offset between RV and transit surveys remained unsettled. A three-day period corresponds to two times the stellar Roche radius, the expected limit of tidal disruption (Rasio & Ford 1996; Owen & Lai 2018). If hot Jupiters formed farther out in the disk and attained heightened eccentricity through planet–planet scattering (or secular chaos; Wu & Lithwick 2011), tidal circularization would force these planets to migrate inward to short periods. This process is truncated by the tidal disruption radius, where orbital crossings tear the planet apart, leading to a population turnover around three days. We observed an occurrence break at $3.4^{+1.9}_{-0.8}$ days for our combined Kepler and K2 Jupiter population, where the increased sample size shifts the break closer to the expected three-day limit. This finding relieves tension between RV and transit demographics, providing a robust measure of the three-day population break with transiting planets and therefore further evidence of high-eccentricity migration.

The longer-period population, known as the period valley (e.g., Wittenmyer et al. 2010), is less clear in its origin. Many studies, including Santerne et al. (2016), observed a dip near 10 days followed by increasing warm-Jupiter occurrence out to 100 days. The inclusion of the K2 sample smooths out this dip, yielding a flat distribution in $\log P$ out to 40 days ($\beta_2 = -0.1 \pm 0.3$). This occurrence plateau is difficult to rectify with high-eccentricity migration since it creates a binomial population of cold and hot Jupiters (i.e., too few warm Jupiters; Wu & Lithwick 2011; Petrovich et al. 2014; Petrovich & Tremaine 2016). Perhaps some combination of disk and high-eccentricity migration blend to form the existing population of warm Jupiters (Dawson & Johnson 2018). Our smoothing of the 3–40 day distribution with the joint Kepler and K2 sample further validates the complex origin of these planets.

It is important to note that metallicity is strongly correlated with hot-Jupiter occurrence (Fischer & Valenti 2005); thus, these populations are significantly skewed toward metal-rich stars. Further discussion of the metallicity dependence is provided in Section 6.2.

6. Trends in Stellar Host Parameters

Here we consider known stellar trends in spectral class ($T_{\rm eff}$) and metallicity ([Fe/H]) and examine how the addition of K2 planets modifies these parameters. The K2 catalog only provides a 19% increase in the total planet sample (from Kepler alone). However, the Scaling K2 sample provides a 28% increase in bright hosts ($m_v < 14$), where ground-based stellar characterization is readily feasible. Capitalizing on this fact, we can refine previous occurrence trends with the addition of K2 planets. We also introduce a new trend that takes into account the host star's galactic oscillation amplitude ($Z_{\rm max}$).

In each subsection, we discuss additional cuts made in the stellar and planet sample to ensure purity in the metallicity and galactic oscillation amplitude measurements. Large homogeneous surveys like Gaia and LAMOST provide sufficient coverage of the parent stellar population, in that a large enough sample is available to accurately retain the full sample's parameter distributions, as shown in Petigura et al. (2018a). However, our quality constraints may impact the overall occurrence normalization. To address this issue, we introduce a correction factor (κ) to preserve the full catalog occurrence

normalization. Further discussion and the derivation of this factor can be found in Appendix B. We use the following model to describe all three parameters:

$$\frac{d^3 n}{dT_{\rm eff}\, d\,[{\rm Fe/H}]\, d\log Z_{\rm max}} \propto \kappa \ \cdot 10^{[{\rm Fe/H}]\cdot\lambda + \frac{T_{\rm eff}}{1000\,K}\cdot\gamma} \ \cdot Z_{\rm max}^{\tau},$$

(4)

where γ, λ, and τ are all tunable parameters. The metallicity term represents a power law accounting for [Fe/H] being a log ratio of the element abundances, as done in previous [Fe/H]-based occurrence calculations (i.e., Fischer & Valenti 2005). We find a similar trend in $T_{\rm eff}$ best replicates the observed population. This unique model may be due to some scaling with Planck's law, but the origin remains unclear. A power law was chosen for $Z_{\rm max}$ out of simplicity and its ability to match the observed population trend. The model provided in Equation 4 assumes independence of these three stellar parameters, which may be too simplistic. In Sections 6.2 and 6.3, we will discuss these possible correlations and their impact on the trends. To optimize this model, we hold the best-fit combined (Kepler and K2) model parameters fixed for each respective planet class to minimize biases introduced by the underlying planet population. The results of our fitting are provided in Table 2.

6.1. Spectral Class

More-massive stars are the product of a more-massive gas cloud contraction and should, correspondingly, host higher-mass protoplanetary disks early in their lifetimes. Observationally, this has been shown by Andrews et al. (2013). Planet occurrence trends may provide insight into this natal state disk, as planets are born out of the stellar residuals. With RV detections, Johnson et al. (2007) found giant planets are more common around massive stars, aligned with expectations that increased disk material inventory enables more planet formation. However, later occurrence analysis using transiting planets found fewer small (super-Earth and sub-Neptune) planets around more-massive stars (Howard et al. 2012; Mulders et al. 2015), indicating disk solids have a more complex relationship with these smaller-planet classes.

In Figure 6, we investigate the impact of stellar spectral class on planet occurrence. Here, we use $T_{\rm eff}$ as a proxy for stellar mass under the guise of established mass–temperature relationships (Kuiper 1938). Many of our targets still lack the proper stellar characterization—via high-resolution spectra—required for robust mass assessment; however, existing photometry allows for reasonable stellar temperature measurements ($\sigma_{T_{\rm eff}} \sim 100\,K$; Hardegree-Ullman et al. 2020). For this test, we set λ and τ to zero, enabling us to use the full catalog sample and avoid contamination from poorly constrained stellar characterization. For the remainder of the analysis performed in this subsection, we will use the full stellar and planet sample.

Within our sample of FGK stars, we found decreasing occurrence for super-Earths ($\gamma = -0.18 \pm 0.02$) and sub-Neptunes ($\gamma = -0.25 \pm 0.02$) with increasing stellar temperature. These known trends are further amplified with the inclusion of K2 planets, providing additional evidence for the anticorrelation of stellar mass and small-planet occurrence. Both populations depict a nearly 75% reduction in planet

Table 2
Parameters for Our Combined Kepler and K2 Stellar Trend Models

Class	Period (days)	γ	λ	τ	Kepler	K2
SE						
	1–40	-0.17 ± 0.02	...	...	802	51
	1–10	-0.41 ± 0.04	0.5 ± 0.1	...	305	37
	10–40	0.01 ± 0.07	0.0 ± 0.2	...	133	4
	1–40	-0.14 ± 0.04	...	-0.30 ± 0.06	367	49
SN						
	1–40	-0.25 ± 0.02	...	...	797	219
	1–10	-0.42 ± 0.05	1.2 ± 0.1	...	160	68
	10–40	-0.28 ± 0.03	0.26 ± 0.09	...	307	104
	1–40	-0.25 ± 0.03	...	-0.37 ± 0.07	322	190
SS						
	1–40	-0.21 ± 0.07	...	...	63	25
	1–10	-0.5 ± 0.2	2.5 ± 0.5	...	11	8
	10–40	-0.23 ± 0.15	1.2 ± 0.4	...	21	8
J						
	1–40	-0.01 ± 0.08	...	...	58	25
	1–10	0.0 ± 0.2	2.6 ± 0.5	...	26	10
	10–40	-0.2 ± 0.03	1.6 ± 0.8	...	6	2

Note. We provide the number of candidates in each respective sample in the two rightmost columns.

occurrence moving from a $T_{\rm eff}$ of 4000 to 6500 K, while the star mass increases nearly 75% across these spectral classes. This counterintuitive trend may be caused by a rise in outer giant formation, cutting off the flow of pebbles to the inner disk and reducing the material available for smaller-planet formation (Mulders et al. 2021).

Stellar trends for transiting giants are difficult to resolve with the Kepler sample alone, given the relatively narrow and peaked stellar parameter space probed by the Kepler host stars (see Figure 7). Using K2, we can significantly improve the resolution of these trends due to the improved coverage of the edges of the stellar parameters probed across the two surveys. Intriguingly, we find decreasing sub-Saturns occurrence around more-massive stars ($\gamma = -0.21 \pm 0.07$). If the mass-loss/disruption mechanism responsible for sculpting the edge of the sub-Saturn desert swells outward to longer periods for high-mass stars, as suggested by Hallatt & Lee (2022), then such evolutionary processes may be responsible for the observed sub-Saturn occurrence reduction.

We also observed a flat occurrence profile for Jupiters as a function of stellar spectral class ($\gamma = -0.01 \pm 0.07$), contrasting with established RV results that found increasing occurrence as a function of stellar mass for M dwarfs (Johnson et al. 2007). However, a more granular examination of our sample shows the population rate is increasing from 4000 to 4500 K followed by a flattening, suggestive of a rise in occurrence from M to K dwarfs. We suspect a wider stellar sample would display the Jupiter planet occurrence steeply increasing up to the early K dwarfs, at which point the occurrence rate flattens. Perhaps this turnover indicates some saturation point, where increasing the disk mass leads to no further hot- and warm-Jupiter planet production. Using TESS, Beleznay & Kunimoto (2022) found evidence of decreasing hot-Jupiter occurrence around more-massive stars (AFG types), which may complicate this narrative; however, this trend remains tentative. We provide further discussion of the implications of this trend in Section 6.2.2. Further analysis

with direct measurements of the stellar host mass will provide a clearer understanding of these apparent trends.

Within our sample there may exist degeneracies in $T_{\rm eff}$ and [Fe/H]. Hotter and more-massive stars tend to be younger and have a higher metallicity. Johnson et al. (2010) showed that a mass–metallicity plane could provide a more robust description of the observed gas-giant population. In Section 6.2 we investigate the impact of composition on planet occurrence while simultaneously fitting for a spectral-class trend. In Section 6.3 we disentangle these two stellar features and resolve a galactic location dependence.

6.2. Metallicity

The natal disk inventory dictates the available building blocks for planet formation. By considering the current stellar abundances, as measured through spectral analysis, we are provided a glimpse into the composition of this natal disk. Early RV studies found strong correlations between Jovian planets and stellar iron (Fe) abundances (e.g., Fischer & Valenti 2005), suggesting Fe is a key component in giant-planet formation. Further analysis of RV planets found the trend weakened for smaller planets (Sousa et al. 2008; Ghezzi et al. 2010), indicating some alternative relationship with the disk iron content. This reduced correlation was corroborated with the Kepler transiting sample (Petigura et al. 2018a), using HIRES and LAMOST spectra to measure the [Fe/H] for a subset of hosts and field stars.

We provide further refinement to this analysis by including planets from the K2 sample. Up until this point, we have been using a sample of stars that contain a mixture of spectroscopically and photometrically derived parameters, but the occurrence models used in Section 5 only relied on quantities well constrained by photometry. [Fe/H] measurements are poorly constrained via photometry. Thus, to ensure a pure sample, we removed targets without available spectra, leaving 22,985 Kepler and 19,084 K2 targets. Correspondingly, the planet sample was reduced to 969 Kepler and 241 K2 planets.
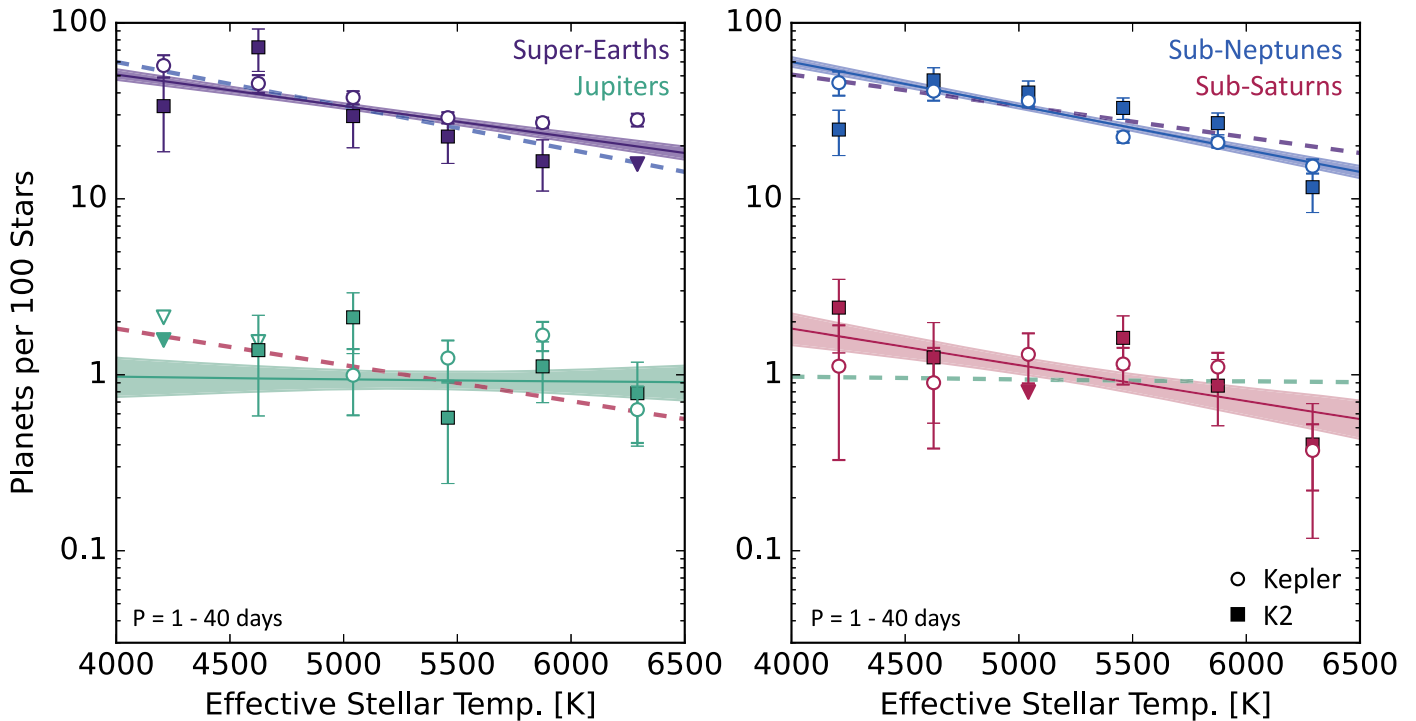
Figure 6. The occurrence for Kepler (circles) and K2 (squares) for each relevant class of planets as a function of effective stellar temperature, which is a proxy for spectral class and disk mass. The best-fit trend lines are displayed with the 1σ model regions shaded. We included the best-fit trend of the adjacent plot as dotted lines for comparison. In this analysis, we set λ and τ to zero to focus on $T_{\rm eff}$ dependencies (γ) and to utilize the full population sample without loss of precision. The trend model parameters are provided in Table 2.

From this pure sample,[25] we can extract meaningful metallicity trends. It is important to note that this cut may systematically change the overall occurrence of any planet class. Thus, an additional correction factor (κ) was introduced to preserve the initial class occurrence (see Appendix B for more details). In optimizing our planet population models for this sample, we set τ to zero, allowing the $T_{\rm eff}$ and [Fe/H] dependence to be assessed without contamination from inaccurate galactic proper motion (PM) measurements.

We previously noted that Equation 4 assumes parameter independence, which may not be accurate. Thus, we examined the posterior chains of $T_{\rm eff}$ and [Fe/H] and found little evidence of covariance among these parameters for any of the planet classes. We do not attempt to rule out any such correlations but note that our assumption of independence was not wildly inaccurate and provides a reasonable model for the associated stellar trends.

In Section 5 we discussed various period breaks in each planet class, ranging from 3 to 10 days. These turnovers in occurrence seem to indicate some underlying physical processes, separating the populations. The exact origin of these population peaks remains unclear, but it seems plausible that either side of these breaks represents planets with unique formation histories. Although we find a range of $P_{\rm br}$ values for each planet class, we chose to separate the planet population at 10 days to offer a direct comparison with the existing literature.

---

[25] Our spectroscopic sample harbors metallicities with uncertainties ranging from 0.004 to 0.15 with a median uncertainty value of 0.03 dex. We did not account for uncertainty in our model optimization but expect the impact to be minimal given the precision of our sample.

6.2.1. Super-earths and Sub-Neptunes

In Figure 8 we display the sub 10 day planet occurrence as a function of stellar iron abundance from our combined Kepler and K2 sample. Super-Earths produce a trend ($\lambda = 0.5 \pm 0.1$) consistent with the results of Petigura et al. (2018a) and Wilson et al. (2022), but with a 50% reduction in uncertainty. These previous studies found a marginally significant trend ($\sim 3\sigma$), but here we confirm to 5σ confidence that hot super-Earths have a positive metallicity dependence. We found similar agreement, with the previous works, for the population of hot sub-Neptunes ($\lambda = 1.2 \pm 0.1$). These two planet classes have similar masses but are differentiated by their outer envelope, suggesting an interconnected formation history. Photoevaporation models (Owen & Lai 2018) expect increased mass loss in lower-metallicity atmospheres, where cooling is less efficient. Hot sub-Neptunes are expected to undergo significant atmospheric removal due to the proximity to their host star, leaving behind a super-Earth with a thin H/He atmosphere. The predicted metallicity dependence is in alignment with our trends, which display a steep increase in the occurrence of hot sub-Neptunes around metal-rich stars. Furthermore, we found a 70% increase in the spectral-class dependence (relative to the trend in Figure 7) in these short-period planets ($\gamma = -0.42 \pm 0.05$), indicating increased luminosity further reduces the sub-Neptune occurrence, an expectation of photoevaporation models. If mass loss completely explained this occurrence trend, we might expect a similar-magnitude negative metallicity correlation for the hot super-Earth population. However, the observed positive occurrence slope for the hot super-Earths is likely due to increased core production at higher disk metallicities, an expectation of core accretion (Pollack et al. 1996). It is clear that multiple mechanisms are at
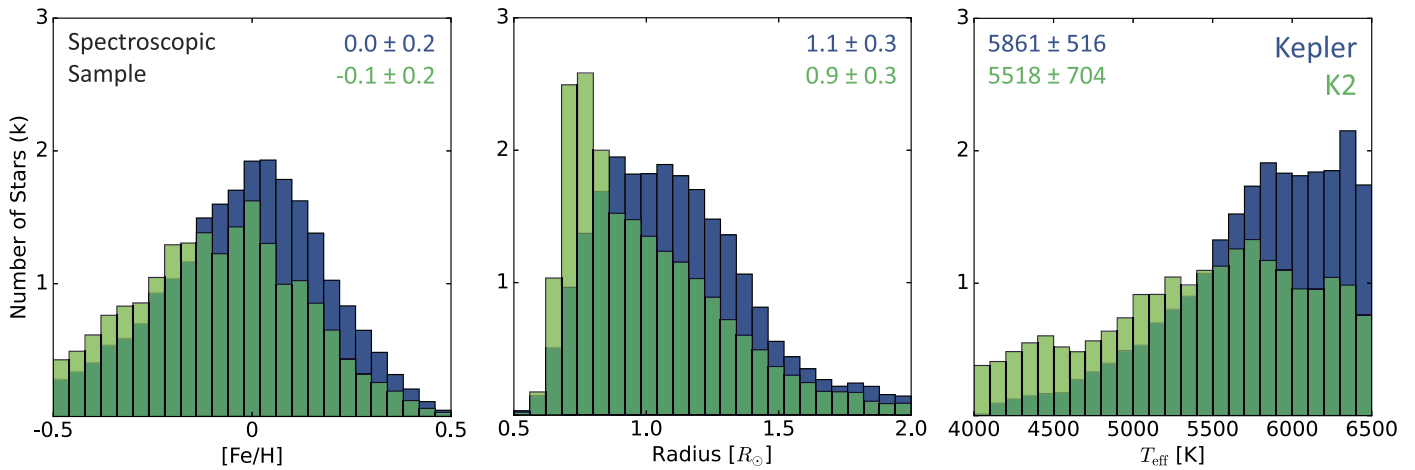
Figure 7. The distribution of our stellar sample with spectroscopically derived parameters. The corresponding distribution median and MAD values are provided in each parameter window.

play within these populations, and further investigation is necessary to parse the magnitude of their effects.

At longer periods (10–40 days; Figure 9), the mass-loss mechanisms carving out the radius valley define our population limits. Thus, occurrence trends in this region should highlight the natal formation of super-Earths and sub-Neptunes. We observed a negligible correlation with [Fe/H] ($\lambda = 0.0 \pm 0.2$) and T_{eff} ($\gamma = 0.01 \pm 0.07$) for warm super-Earth occurrence. Sub-Neptunes present a slight correlation with stellar metallicity ($\lambda = 0.26 \pm 0.09$) while maintaining a significant spectral-class dependence ($\gamma = -0.28 \pm 0.03$). These trends are in agreement with previous studies (Petigura et al. 2018a; Wilson et al. 2022), which measured [Fe/H] effects using a wider period range (10–100 days). Again, we reduce the uncertainties by ∼50%, further flattening the warm super-Earth trend. If standard core accretion is responsible for these correlations, we would expect more-massive cores around metal-rich stars, increasing sub-Neptune production while reducing super-Earth occurrence. Therefore, the flattening of the super-Earth trend provides tension here. Perhaps metal-driven cooling effects saturate at longer periods, and these super-Earths represent a population of planets born with thin H/He atmospheres. Rogers & Owen (2021) found that ∼20% of the super-Earth population formed with a thin envelope, contrasting the primary expectation of an atmospheric mass-loss origin. Furthermore, the isothermal cooling limits for super-Earth-sized cores ($1–2M_{\oplus}$) provide a ceiling on the natal gas accretion, predicting the existence of a robust population of longer-period primordial super-Earths, where mass-loss processes are impotent (Lee & Connors 2021). Intriguingly, our models suggest warm super-Earth cores are formed independently of the stellar host-star parameters, while sub-Neptune production decreases for more-massive early-type stars. In Section 7.1 we discuss this difference and the implications for formation. Close visual inspection of the warm super-Earth and sub-Neptune occurrence values suggests a broken power law may be more appropriate in modeling their metallicity dependence, further complicating their underlying genesis. We leave such analysis for future studies.

6.2.2. Gas-giant Metallicity Trends

Our sample of K2 sub-Saturns and Jupiters provide an additional 16 and 12 planets, respectively. Since the existing

Kepler population only consists of 32 sub-Saturns and 32 Jupiters, this significantly increases the available sample. Compared to the smaller-planet classes, we find a stronger metallicity trend for the gaseous hot sub-Saturn ($\lambda = 2.5 \pm 0.5$) and hot-Jupiter populations ($\lambda = 2.5 \pm 0.4$), in agreement with previous Kepler-based work (Buchhave et al. 2012; Petigura et al. 2018a; Wilson et al. 2022). Our reduced uncertainties bring these two population trends into alignment, indicating a similar disk metallicity dependence. Furthermore, we find a hot-Jupiter correlation in agreement with previous RV surveys of the local solar neighborhood ($\lambda = 2.1 \pm 0.7$; Guo et al. 2017), strengthening this result.

Our 10–40 day populations indicate a consistent metallicity dependence for the warm sub-Saturns ($\lambda = 1.2 \pm 0.4$) and the warm Jupiters ($\lambda = 1.6 \pm 0.8$). We observed a trend reduction when compared to their short-period counterparts and witness alignment with long-period RV trends (Johnson et al. 2010; $\lambda = 1.2 \pm 0.2$). Beyond 10 days, it appears sub-Saturns are 3× more likely to occur than Jupiters. This is in conflict with standard formation models (Pollack et al. 1996), which expect runaway accretion to take over in the sub-Saturn core-mass range ($\sim 10M_{\oplus}$). Mass-loss mechanisms like photoevaporation (Hallatt & Lee 2022) should have a greater impact on the short-period population, but we find this excess is unique to planets orbiting beyond 10 days, suggesting some primordial formation effects. Further discussion of this offset is provided in Section 7.2.1.

It may be that the disk itself is throttling the production of more-massive warm Jupiters, but we find no evidence of any spectral-class dependence—which provides a proxy for stellar and disk mass—when simultaneously fitting for metallicity ($\gamma = -0.2 \pm 0.3$). It seems that metallicity is the driving mechanism in the production of warm Jupiters, and the disk mass is not a major limiting factor. Understanding the mechanism for this surplus will provide significant insight into sub-Saturn planet formation.

Overall, we find similar results to existing planet metallicity trends, but our inclusion of K2 planets shows convergence in the trends for giants and smaller planets.

6.3. Galactic Oscillation Amplitude

Galactic location remains of interest in planet formation given the unique element inventory of the differing galactic
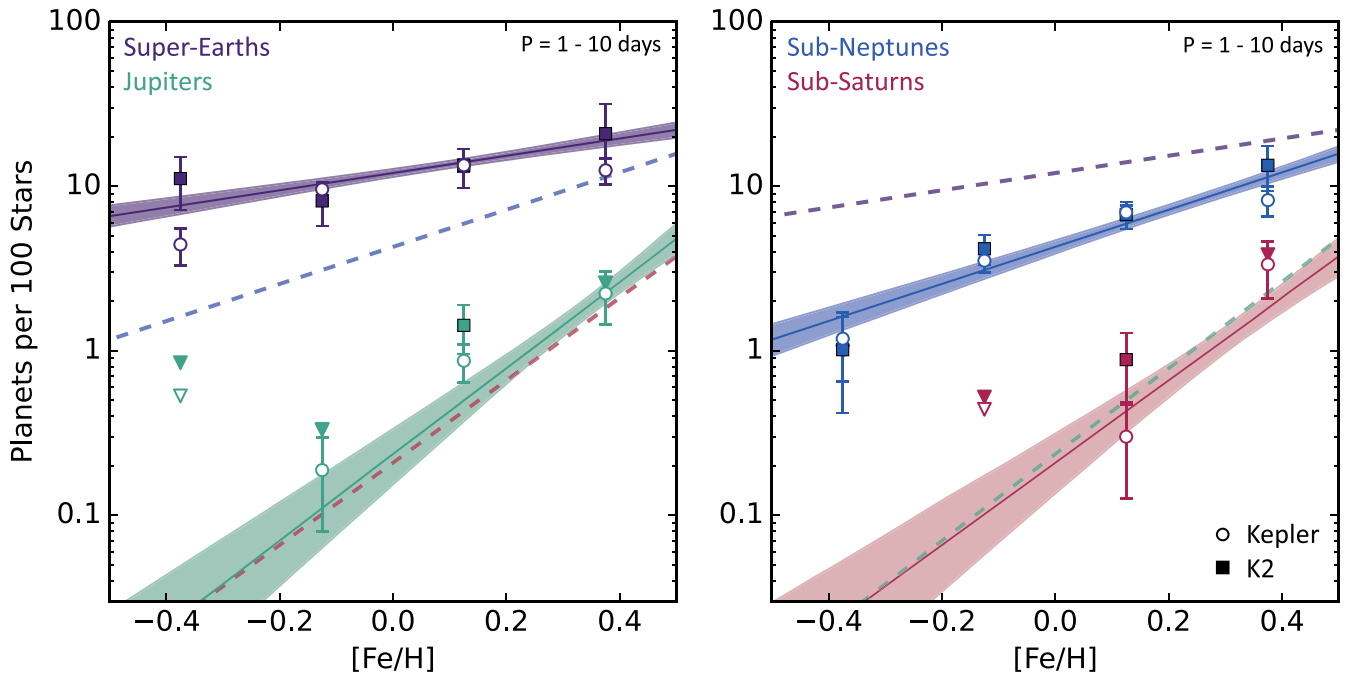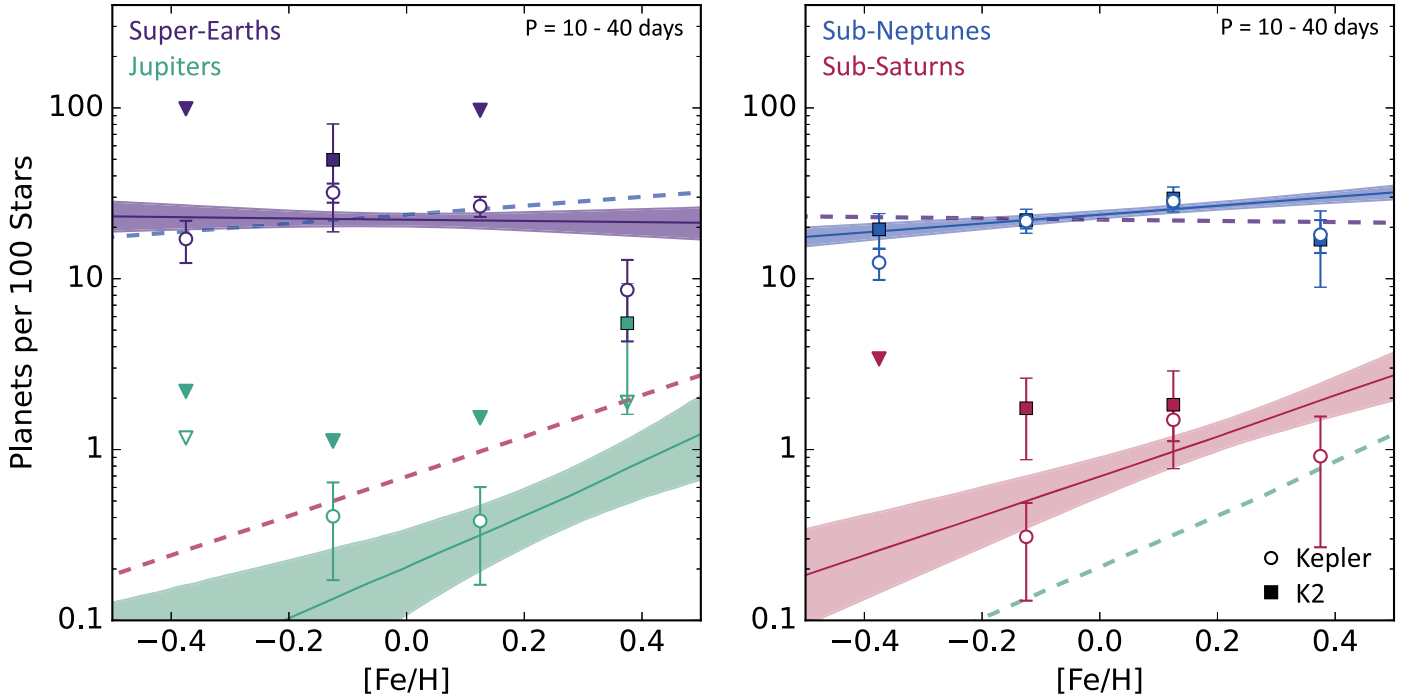
Figure 8. The occurrence of short-period (1–10 days) Kepler (circles) and K2 (squares) planets as a function of [Fe/H]. The triangle shapes represent 3σ upper limits for the respective bin. The best-fit trend lines are displayed with 1σ model regions shaded. To highlight similarities between planet classes, we display the best-fit models of sub-Neptunes and sub-Saturns as dotted trends on the right panel. Likewise, we display super-Earth and Jupiter dotted trends on the left panel. The model parameters are provided in Table 2.

substructures. Thick-disk stars have reduced iron and enhanced alpha-element abundances, a product of Type II supernova dominance during the formation of these older stars (Wallerstein 1962). Furthermore, halo stars are a mixture of very metal-poor (older) stars diluted by a population of alpha-enhanced (younger) stars, likely the outcome of young satellite population capture (Venn et al. 2004). Radially, a negative metallicity trend has been identified (e.g., Cheng et al. 2012), indicating stars near the galactic center are metal rich compared to stars in the local solar neighborhood. These galactic substructures also harbor unique birth environments that may dynamically interact with planetary systems. For example, many halo stars were born in dense globular clusters (Harris 1976) where an abundance of stellar interactions can produce complex planetary systems (i.e., Spalding & Batygin 2014).

The current planet population is the outcome of natal disk composition and a history of dynamic interactions. Since stars are not born in isolation, but rather part of a dynamic galaxy, their location may provide a fossil record of planet formation throughout the history of the Milky Way, unveiling long-term formation processes and pathways not seen in younger planet populations. McTier & Kipping (2019) examined the spatial planet occurrence of Kepler hosts by considering Gaia DR2 galactocentric velocities, finding that all differences between the host and nonhost populations could be explained by selection effects. Chen et al. (2021) used LAMOST spectra and found a slight decrease in system multiplicity for thick-disk hosts, suggesting an increased rate of instabilities for these older systems. Using TESS, Kolecki et al. (2021) and Boley et al. (2021) constrained the hot-Jupiter population in the metal-barren halo to less than 0.18%, predicting a minimum [Fe/H] formation threshold between −0.7 and −0.6 dex. Using the combined Kepler and K2 sample, along with PM

measurements from Gaia DR3 (Gaia Collaboration et al. 2022), we examined our planet sample for trends in stellar location.

A star's current position, relative to the galactic disk, can be determined by sky coordinates and parallax distance. However, these distances are merely a snapshot of their oscillation trajectory about the disk midplane. The amplitude of this oscillation is the characteristic that dictates the substructure membership (thin disk versus thick disk). Previous work has used kinematic properties to assign membership probability (Chen et al. 2021), binning the stellar population into separate substructures. This method is robust and attainable for nearly all stars in the Kepler sample. However, it fails to capture subtle trends that may be convoluted due to the dynamic diffusion and kinematic mixing of these discrete populations (Rix & Bovy 2013). We chose to consider a direct measure of the fully integrated orbital oscillation amplitude, using Gaia DR3 PM and RV measurements (Katz et al. 2022). To ensure consistency, we required all targets in this section to have measured Gaia RVs and PM measurements. Implementing the Gala software (Price-Whelan 2017) to model the stellar orbits about the galactic disk, we used a simple mass model for the Milky Way (derived in Bovy 2015). All stars then underwent 100 simulated oscillations about the disk, varying the PM and RV values according to the stated uncertainties to achieve a measure of amplitude precision. We then removed all targets with amplitude uncertainties greater than 10% to maintain purity (see Figure 10). Furthermore, we focused on targets with semiamplitudes greater than 100 pc and less than 1000 pc since this range contains a majority of the planet sample and emphasizes the transition from thin- to thick-disk stars. The parameter distribution of this astrometrically pure sample is provided in Figure 11, and a corresponding Toomre velocity diagram of our astrometric stellar sample is shown in Figure 10. This astrometric filtering removes 83,304 targets and 1075 planets from our sample. As previously

Figure 9. The occurrence of warm (10–40 days) Kepler (circles) and K2 (squares) planets as a function of [Fe/H]. The triangle shapes represent 3σ upper limits for the respective bin. The best-fit trend lines are displayed with 1σ model regions shaded. The trend values are provided in Table 2.
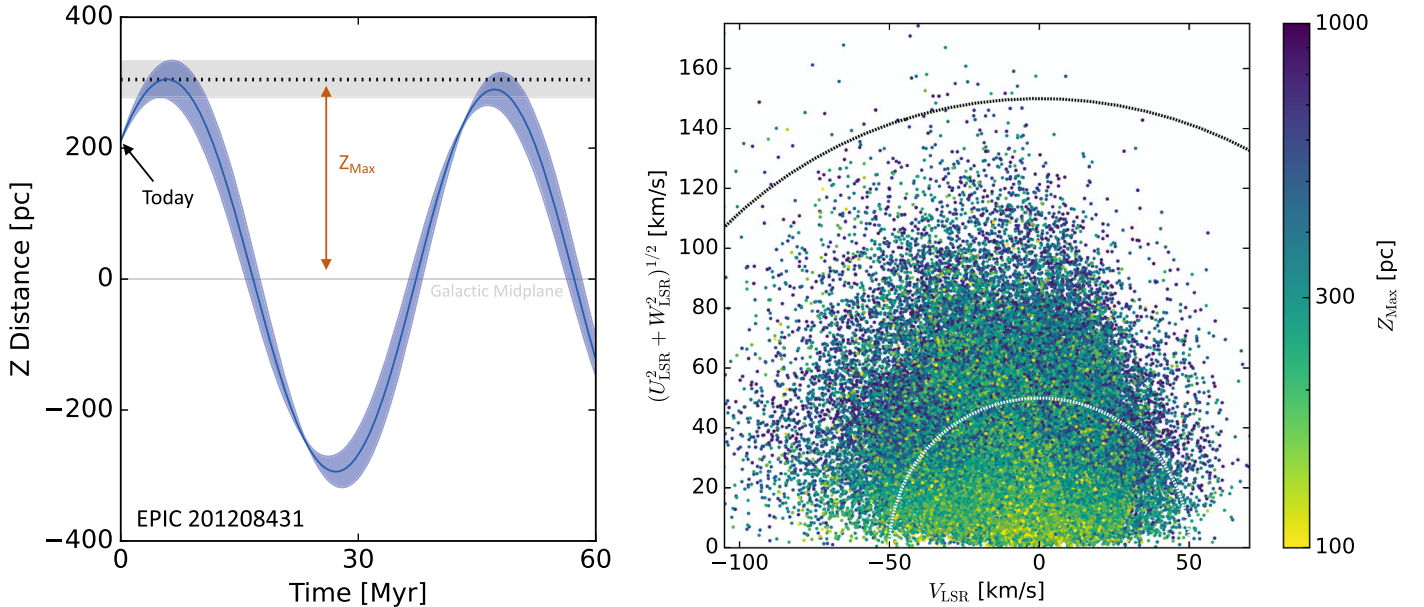

Figure 10. Left: an example of our galactic oscillation simulation for EPIC 201208431, showing how we derived our stellar-amplitude values. Using the `Gala` software, in conjunction with the Gaia DR3 proper motion and radial velocity parameters, we simulated each star's oscillation (dark blue line) about the galactic midplane, measuring the star's amplitude (Z_{Max}). We then repeated this N-body simulation 100 times, varying the Gaia values within their uncertainty ranges. The oscillation 1σ range is displayed in light blue, and the uncertainty in Z_{Max} is shown in light gray. The right panel displays the corresponding Toomre diagram for our astrometric stellar sample. U, V, and W velocities were calculated in the local standard of rest frame (LSR). The 50 and 150 km s^{-1} total relative velocities have been provided as loose bounds for the thin and thick disks, respectively. In general, our integrated orbital Z_{Max} values map onto this diagram as expected; low-Z_{Max}, thin-disk stars have a much lower total relative velocity than their high-Z_{Max}, thick-disk counterparts.

mentioned, these cuts may impact the overall occurrence normalization; thus, a correction factor was implemented (see Appendix B for details).

In Figure 12 we present the trend for Z_{Max} as a function of planet occurrence for the super-Earth and sub-Neptune host populations. Overall, we found reduced planet occurrence at higher galactic amplitudes. As pointed out in McTier & Kipping (2019),

such galactic trends may be the outcome of sample selection effects. To address this issue, we simultaneously fit for T_{eff} and observed that this trend remains significant—super-Earths: $\tau = -0.30 \pm 0.06$; sub-Neptunes: $\tau = -0.36 \pm 0.07$. It is expected that stellar metallicity will decrease moving up in amplitude, naturally reducing planet occurrence. However, limiting the sample to stars with spectroscopic metallicities and precise astrometry
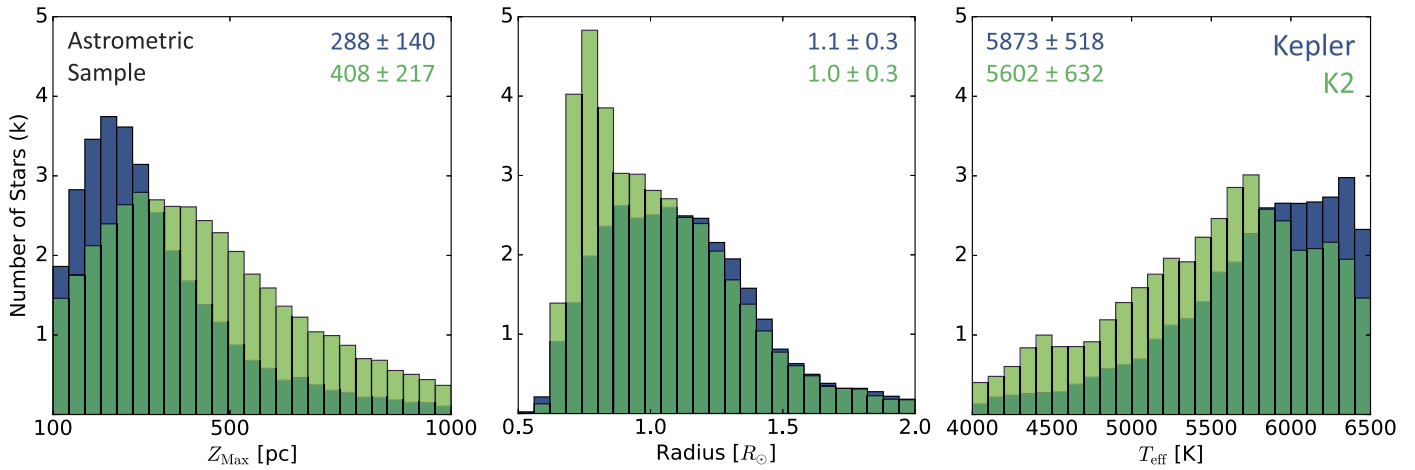
Figure 11. The distribution of our stellar sample with precise astrometric parameters available. The corresponding distribution median and MAD values are provided in each parameter window.

reduces the planet sample to a nonstatistical level. Instead of a direct simultaneous fit with stellar [Fe/H], we measured the expected metallicity–amplitude trend in the overlapping spectroscopic and astrometric stellar samples, finding a slope of -0.275 dex kpc^{-1}. Schlesinger et al. (2014) carried out a large survey of galactic chemistry gradients and found a weaker -0.243 dex kpc^{-1} trend, indicating our derived gradient is likely over-representing the effect of metallicity. We then computed the expected occurrence–metallicity correlation for the full 1–40 day period range, yielding λ values of 0.24 ± 0.06 for the super-Earths and 0.34 ± 0.05 for the sub-Neptunes. Putting these trends together, we conservatively estimated a super-Earth and sub-Neptune population reduction of $14\% \pm 3\%$ and $19\% \pm 2\%$, respectively, over the first kiloparsec above the galactic plane due to metallicity alone. This is significantly less than the $50\% \pm 8\%$ and $56\% \pm 7\%$ occurrence drop seen for the super-Earth and sub-Neptune populations. In other words, we find a greater than 4σ difference between our conservative metallicity estimate and the observed trends, indicating an alternative mechanism must account for the lack of high stellar-amplitude planets. It is important to note that we forced λ to be zero for this optimization and that a more thorough accounting of the correlations between [Fe/H] and Z_{Max}, with a well-parameterized stellar sample, may yield a reduced τ value. However, our quantification of the expected [Fe/H] contributions shows that the existence of even a strong correlation between location and metallicity will not rectify the detected Z_{Max} trend. The physical amplitude is likely a proxy for some other parameter, like stellar age, but it is clear that the [Fe/H] and T_{eff} trends are not sufficient in replicating the observed occurrence rate gradient. In Section 7.3, we provide further remarks on the potential origin of this galactic trend.

7. Discussion

7.1. Small-planet Differences

Our combined analysis of the Kepler and K2 planet samples used an empirically derived super-Earth and sub-Neptune boundary. Doing so, we found the occurrence of super-Earths and sub-Neptunes turns over at 5.6 ± 1.1 and 9.5 ± 2.0 days, respectively. This is a reduction in the period break reported by Petigura et al. (2018a), who found $P_{\mathrm{br}} = 6.5^{+1.6}_{-1.2}$ and $P_{\mathrm{br}} = 11.9^{+1.7}_{-1.5}$ days for the super-Earth and sub-Neptune populations, respectively, when drawing a strict radius partition

($1.7R_\oplus$). Using a functional class boundary provides a more accurate classification of these small planets and brings the population P_{br} values in closer alignment. The turnover difference in these two populations is expected due to mass-loss mechanisms, which remove H/He atmospheres from sub-Neptunes, increasing the short-period super-Earth population.

It is also notable that the occurrence of super-Earths decreases beyond this break. Previous work found a negligible slope beyond 10 days due to heavy contamination from small-radius sub-Neptunes (i.e., Petigura et al. 2018a). Our upper radius valley and lower $1R_\oplus$ bound may also be responsible for this drop, narrowing the parameter space available for the long-period population. If sample completeness was significant below $1R_\oplus$ and we extended our definition of super-Earths to include sub-Earths, we may expect the long-period occurrence slope to align with the sub-Neptune population. However, Qian & Wu (2021) found an inflection around $1R_\oplus$, suggesting sub-Earths represent a unique population that is not an extension of super-Earths. These planets are likely born intrinsically rocky and are not the outcome of atmospheric mass loss (Owen & Lai 2018; Neil & Rogers 2020). Therefore, the occurrence of planets born as sub-Neptunes, which underwent atmosphere erosion, does indeed appear to drop at longer periods where mass-loss mechanisms decay in efficiency.

In Figure 9, the warm super-Earth and sub-Neptune populations appear to be independent of stellar metallicity. Furthermore, warm super-Earths present an insignificant correlation with spectral class, while warm sub-Neptune occurrence decreases around earlier-type stars. Petigura et al. (2022) found increasing sub-Neptune radii around more-massive stars, while super-Earths maintain uniformity across a wide stellar-mass range. Assuming a constant critical core-mass threshold, where planets with cores below this limit undergo photoevaporation, a single core distribution can reproduce this population difference if more-massive stars produce a wider dynamic range of planetary cores (see Figure 15 of Petigura et al. 2022). Our stellar independence for warm super-Earths and spectral dependence for warm sub-Neptunes is in alignment with this model. Warm super-Earth production appears to saturate around FGK stars, where sufficient material is available for the primordial core distribution to exceed the critical core-mass threshold. In contrast, sub-Neptunes likely undergo luminosity-based mass loss and leave behind thick H/
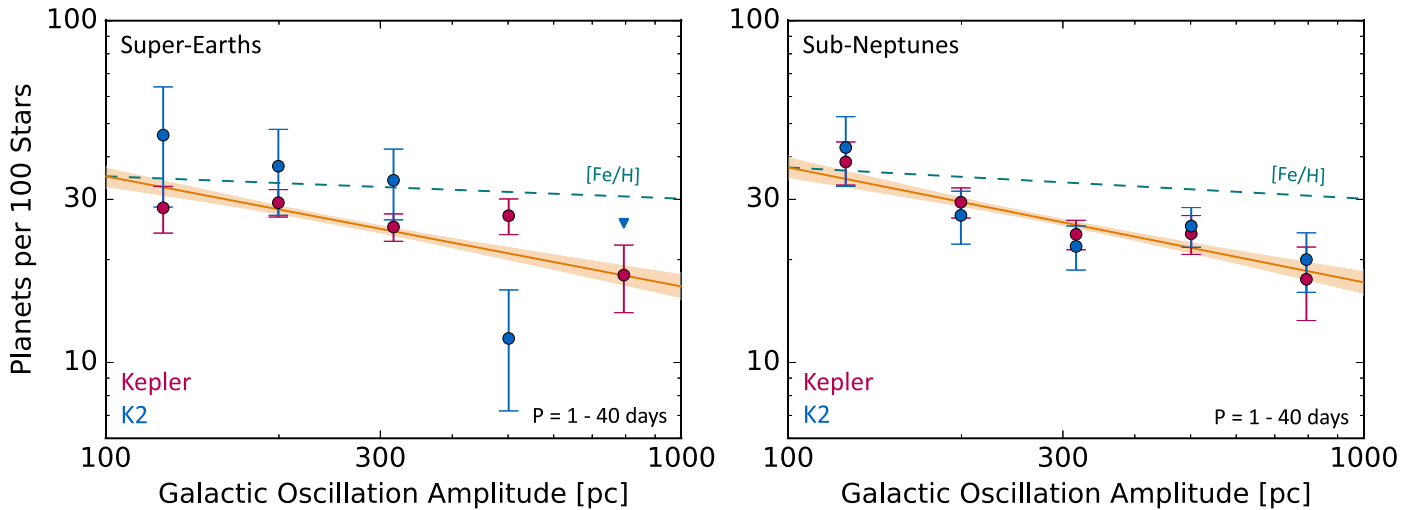
Figure 12. The occurrence of super-Earths and sub-Neptunes as a function of stellar galactic oscillation amplitudes (Z_{Max}). The orange trend lines denote the best-fit model and the 1σ confidence interval. The teal dotted trend illustrates the occurrence expectation from our calculated galactic [Fe/H] gradient. The triangle shapes represent 3σ upper limits for each bin. We note that the displayed binned Kepler and K2 occurrence values are meant to portray the underlying raw occurrence. The model parameterization was performed within our forward-modeling framework using a binless CDF optimization.

He envelopes around only the highest-mass portion of the core population.

Overall, super-Earths present a flattened distribution in log-period space. If these thin envelope planets provide a more pristine portrayal of the underlying core distribution, this population compression provides further evidence of a log-uniform period core distribution, as suggested by unified primordial core models (i.e., Rogers & Owen 2021). Despite the differences observed between these two populations, it appears that mass loss remains a competent theory for explaining deviations, under the guise of a single birth population.

7.2. Small Planets and a Common Birth Population

Previous demographic work has shown that a majority of super-Earths hail from a core population common with that of sub-Neptunes (Rogers & Owen 2021). If correct, we should expect stellar trend similarities when marginalizing over the full range of periods where mass-loss mechanisms are relevant. In other words, if both populations form from a single primordial core distribution, the initial core draw should be consistently dependent on the intrinsic system characteristics. Fortunately, the K2 sample probes exactly the relevant range —beyond 40 days sub-Neptune mass loss is negligible. In Figure 6, we show consistency between these two planet classes and their association with spectral class. However, a trend reduction ($\Delta\gamma = -0.08 \pm 0.03$) is noted between the super-Earth and sub-Neptune populations, providing tentative evidence for a stellar-driven mass-loss mechanism, in contrast with primordial super-Earth formation (Lee & Connors 2021). Rogers et al. (2023) made a similar occurrence ratio argument using stellar mass and found a consistent trend. Alternatively, this difference may highlight a more complex primordial core distribution.

In Figure 4, a significant deviation in these two planet classes is observed for periods within 10 days. Here, atmospheric mass-loss mechanisms, which are dependent on envelope opacity and metallicity (see Owen & Lai 2018), are largely at play. This expected population difference is reflected in the metallicity trend sub 10 days (Figure 8). The super-Earth

population depicts the impact of metallicity on the primordial core production, while the increased metal trend in the sub-Neptunes highlights the improved atmosphere retention in metal-rich envelopes. The [Fe/H] correlation for these two classes flattens beyond 10 days, but T_{eff} remains an important parameter in warm sub-Neptune occurrence as discussed in Section 7.1.

We also find similarity in the galactic amplitude trends (super-Earths: $\tau = -0.30 \pm 0.06$; sub-Neptunes: $\tau = -0.36 \pm 0.07$), suggesting the galactic component responsible for this trend is agnostic to sub-Neptunes over super-Earths. The summation of these stellar trends points to a common core birth population.

7.2.1. Warm Sub-Saturn Origins

The origin of sub-Saturns remains mysterious, as their similar-period integrated occurrence with Jovian planets is in tension with standard core-accretion planet formation (Pollack et al. 1996). In Figures 4 and 5, the overall shape of the sub-Saturn period population mimics that of the sub-Neptune distribution, with a sharp occurrence increase up to 10 days followed by a slight reduction. This excess of warm sub-Saturns is not replicated in the Jovian population, indicating some unique formation pathways. Furthermore, stellar spectral class appears to play a role in sub-Saturn planet occurrence, whereas no apparent dependence is observed for the Jovian population (see Figure 6). Perhaps this population of warm sub-Saturns is the tail end of the sub-Neptune core distribution. Recent RV follow-up studies have found these warm sub-Saturns harbor a range of eccentricities (e.g., Nowak et al. 2020); thus, it seems plausible that the most-massive sub-Neptune cores may have undergone some tidal radius inflation (Millholland et al. 2020).

We found a consistency of roughly 1σ in our combined period population models (β_1, P_{br}, and β_2) for the sub-Neptune and sub-Saturn planet classes, providing evidence for an interconnected history. Furthermore, we observed a heightened power-law dependence for the sub-Saturn radius population ($\alpha = -2.7 \pm 0.6$) when compared to the sub-Neptunes ($\alpha = -1.7 \pm 0.1$). If these two planet classes share a common origin, tidal inflation would skew the underlying radius

distribution toward smaller planets. In other words, if we assume core masses over some threshold ($\sim 10 M_\oplus$) undergo runaway accretion and form Jovian planets, cores short of this threshold may experience tidal inflation. This radius enhancement creates a steep population decline in the radius distribution beyond the corresponding mass limit (see Figure 5 of Millholland et al. 2020).

Simultaneously, the properties of some sub-Saturns cannot be rectified with tidal inflation; for example, Kepler-1656b is a $5 R_\oplus$ planet with a mass of $48 \pm 4 M_\oplus$ (Brady et al. 2018). These more-massive sub-Saturns exhibit heightened eccentricity and are usually found in single-planet systems (Petigura et al. 2017b), suggesting a planet–planet scattering or merger-based origin after disk dispersal. If the most-massive sub-Saturns form through collisions of smaller-planet cores, the successor distribution may loosely replicate the underlying progenitor population (i.e., sub-Neptunes) with a normalization reduction dictated by the merger efficiency. The consistency observed between the sub-Saturn and sub-Neptune planet population models, and the reduced overall occurrence of sub-Saturns, remains consistent with this formation mechanism.

Our population models suggest less-massive sub-Saturns are an extension of the sub-Neptune population. If the most-massive sub-Saturns, which have a unique eccentricity and multiplicity distribution, are born through collisions of smaller planets after disk dissipation, our population model also remains consistent with this mechanism. Thus, these two independent formation processes are congruent and yield a coherent population trend that mimics the sub-Neptune population, as observed in our model. Alternatively, giant impacts during planet formation may be sufficient in removing large gaseous envelopes, hampering runaway accretion (Biersteker & Schlichting 2019). Nevertheless, it is apparent that the sub-Neptune and sub-Saturn planet populations have an interconnected formation history.

7.3. Possible Causes of the High Galactic Oscillation Amplitude Deficit

In Section 6.3 we found a decrease in super-Earth and sub-Neptune occurrence around stars with large galactic oscillation amplitudes. This result is in alignment with Chen et al. (2021), who found a reduction in planet multiplicity in thick-disk stars. Our trend captures a smooth transition between the thin- and thick-disk populations, circa 300 pc. Either these two stellar populations are not distinct (Park et al. 2021), or they have undergone thorough mixing (Buck et al. 2020) as put forth by galactic simulations.

Regardless of the galactic substructure origin, high-amplitude stars have undergone some additional dynamic heating. Kinematic studies of substructure populations observed a 25% binarity increase in the thick-disk compared to thin-disk stars (Niu et al. 2021), pointing to enhanced fragmentation in older metal-poor star-forming clouds (Tanaka & Omukai 2014). If these high-amplitude stars were born in dense stellar clusters, increased dynamical interactions may play a role in the reduced planet occurrence. However, the period range relevant to this sample is deep within the stellar gravitational potential, requiring a very close flyby encounter or some complex instability triggered by the perturbation of an outer giant planet.

The disk element inventory of thick-disk stars contains a definitively increased relative alpha-element abundance as compared with thin-disk stars. Mg and Si are abundant alpha

elements in terrestrial solar system planets and have condensation temperatures comparable to Fe (Lodders 2003), making them important components of dust in planet-forming regions (e.g., Gonzalez 2009). Additionally, Adibekyan et al. (2012) found a correlation between planet occurrence and [Ti/Fe] abundances, suggesting Fe-poor stars could still efficiently produce planets as long as the Ti abundance was sufficiently high. Within the Kepler sample, Brewer et al. (2018) showed that the relative occurrence of small multiplanet systems increases in the low-[Fe/H] stellar population, indicating non-Fe elements are largely responsible for their formation. Despite these expected correlations with planet occurrence and alpha abundances, we found that the total population of small planets is reduced in the thick disk where alpha elements are more dominant. Counterintuitively, an excessive formation rate could lead to large-scale instabilities that eject most of the small short-period planets (Goldberg et al. 2022) and lead to an overall reduction in occurrence for the alpha-element-rich systems. It may also be the case that the total metal inventory in these high-amplitude stars is lower than in thin-disk stars, making formation inefficient. In other words, thick-disk stars on average only have 50% ([α/H] ~ -0.3 dex) of the total alpha-element abundance of thin-disk stars, despite their dominance over Fe ([α/Fe] ~ 0.3 dex). If these elements are key to small-planet emergence, this deficit may throttle their formation in the thick disk.

Our occurrence measurements assume an isotropic distribution of inclinations. Perhaps the high-amplitude stars have some preferential alignment with the galactic plane. This would manifest in an occurrence deficit (or surplus depending on the direction of the preference) in our calculated values despite a consistent underlying population. While it is difficult to completely rule out this scenario, the nearby binary population suggests no such inclination anisotropy (Agati et al. 2015). Therefore, it is unlikely that high-amplitude planetary systems harbor an orbital preference.

Looking at the giant-planet population may provide hints as to the root cause of this deficit. Unfortunately, our limited sample of astrometrically resolved giant hosts (38 sub-Saturns and 42 Jupiters) does not yield a meaningful trend in the $Z_{\rm Max}$ axis. It may be the case that these gas giants are not impacted by the underlying mechanism responsible for the reduced occurrence of super-Earths and sub-Neptunes. Alternatively, these planets may play a role in the absence of smaller planets (i.e., through dynamic instabilities). Without a larger statistical sample of giant planets, it is difficult to determine their significance in this process. Large missions like TESS (Ricker et al. 2015) and PLATO (Rauer et al. 2014) will provide additional homogeneously identified planet samples that can resolve any existing trends in these giant populations.

8. Summary and Conclusions

We provide a summary of the work presented in this study:

1. Here, we carried out a homogeneous analysis of the Kepler and K2 planet population around FGK dwarfs. In concert, we provided spectroscopic updates to 310 K2 targets using Keck/HIRES, refining the parameters of the underlying stellar population. Overall, we found consistency across all four planet classes (super-Earth, sub-Neptunes, sub-Saturns, and Jupiters). The K2 fields

span a much wider portion of the sky, testing various regions of the local galaxy. Analogous occurrences across these fields and the Kepler postage stamp indicate relatively homogeneous planet occurrences across the local galaxy, further proving the robustness of the Kepler results.

2. This work looked at a range of planet classes and aimed to understand the underlying formation mechanisms that carve out each planet population. Standing on the shoulders of previous demographics work, we separated super-Earths and sub-Neptunes along their expected mass-loss transition. This careful planet classification led to a more flattened period distribution for the super-Earths, aligning with expectations from primordial core models.

3. Testing key results from Kepler , we strengthen trends in stellar spectral class and metallicity. We found super-Earths, sub-Neptunes, and sub-Saturns all diminish in occurrence at higher stellar $T_{\rm eff}$, consistent with previous results, suggesting an inverse formation scaling with disk mass. A flat spectral dependence is found for the Jupiter planet class, indicating some disk mass formation saturation in the FGK mass regime. We also observed consistency with existing metallicity trends, with minor changes bringing the small- and giant-planet correlations in alignment. The consistency in stellar trends for the sub-Neptunes and super-Earths provides further evidence that these two planet populations were born out of the same core-mass distribution, which underwent apparent envelope mass loss.

4. We observed a $3\times$ increase in the occurrence of sub-Saturns relative to Jupiters beyond 10 days. This suggests a distinct formation history. Since mass-loss mechanisms are more potent at short periods, it seems likely that some primordial formation process is responsible for this excess. Our finding also provides further support for a warm-Jupiter valley (a deficit or flattening of occurrence between 10 and 100 day periods). We observed that the sub-Neptune and sub-Saturn period population models are consistent to within 1σ and that the $T_{\rm eff}$ dependence is consistent to 0.5σ, suggesting some interconnection between the formation of these two populations.

5. Using Gaia DR3 PM and RV measurements, we find a striking trend in planet occurrence as a function of the stellar galactic oscillation amplitude. Moving up in amplitude, the number of super-Earths and sub-Neptunes with periods of 1–40 days decreases, suggesting a unique history for the high-oscillation-amplitude planet population. If the galactic amplitude is a proxy for stellar age, as expected by galactic substructure modeling, it may be that long-term dynamical instabilities are responsible for the lack of small short-period planets. Additionally, thick-disk stars have unique element abundance profiles that may contribute to the detected trend. Regardless of the specific dynamics or formation processes responsible for this trend, it is clear that galactic features are imprinted on the planet population. Mapping these galactic influences will provide more robust demographics and a better understanding of our place in the galaxy. The forthcoming Roman space telescope will attain high-cadence photometry for different parts of the local galaxy, with a focus on the galactic bulge. This mission will search a

poorly constrained population of planets, which orbit stars near the center of our galaxy. Here, the stellar metallicity gradients (both radially and vertically) are steeper and the stellar density is heightened, potentially modifying the natal disk composition and each system's dynamic history. The results of this survey will provide a more refined understanding of the interplay between planets and the galaxy they inhabit.

Appendix A
New HIRES Spectroscopy for K2 Targets

Our new sample of HIRES spectra is derived following the procedure of the California-Kepler Survey. We provide a brief summary of the processing undergone to attain our sample of stellar parameters but suggest interested readers reference Petigura et al. (2017a) for a detailed account.

All 456 K2 targets were observed using HIRES on Keck (Vogt et al. 1994) over the course of 2014–2023. This nearly decade-long survey maps well to the release of K2 campaigns as part of the California Planet Search (CPS; Howard et al. 2010), with recent additions following the release of the Scaling K2 homogeneous planet catalog (Zink et al. 2021). The goal of this release is to provide a homogeneous sample of K2 spectra analogous to that of the CKS sample. Our quality requirements are a signal-to-noise ratio $\geqslant 45$ px^{-1} with a corresponding $R \geqslant 60{,}000$, achieved using the "C2" slit.

Processing of these spectra was done using SpecMatch-synthetic (Petigura 2015) for stars with $T_{\rm eff} > 4700$ K (284 stars). This software interpolates over a collection of synthetic spectra in grids of $T_{\rm eff}$, $\log g$, and [Fe/H], modifying the model spectra to reflect the instrument profile, stellar turbulence, and stellar rotation. This grid of modified model spectra was then compared against the target spectra using an L_2 regularization process, yielding characteristic $T_{\rm eff}$, $\log g$, [Fe/H], $v \sin i$ and $M_\star$ values. For stars with $T_{\rm eff} < 4700$ K (26 stars), the synthetic models fail to capture the complex molecular features that arise in real spectra, reducing the software's accuracy. For these stars, we instead used SpecMatch-empirical (Yee et al. 2017), which uses a set of 404 real spectral standards with well-defined $T_{\rm eff}$, $R_\star$, and [Fe/H] parameters to create the model grid. This empirical library captures the complexities that arise in nature, avoiding the model mismatch identified for these cooler stars. The same L_2 regularization process was carried out as SpecMatch-synthetic, producing empirically derived $T_{\rm eff}$ and [Fe/H] parameters.

Table 3
A List of HIRES/isoclassify Stellar Parameters Updates

EPIC	$T_{\rm eff}$ K	$\log g$ dex	[Fe/H] dex	$M_\star$ $M_\odot$	$R_\star$ $R_\odot$	$\rho_\star$ gcc^{-1}	Host
201295312	5837	4.06	0.18	1.17	1.55	0.31	1
201338508	4066	4.70	−0.47	0.56	0.55	3.26	1
201345483	4352	4.58	0.24	0.73	0.72	1.93	0
201357835	5783	4.30	−0.43	0.91	1.13	0.62	0
201384232	5692	4.55	−0.10	0.92	0.89	1.27	1

(This table is available in its entirety in machine-readable form.)

For stellar mass, radius, age, and density parameters, we rely on isochrone grid matching using spectral characterization, PM measurements, photometry, and galactic 3D dust maps. For this optimization, we implemented the isoclassify (Huber et al. 2017; Berger et al. 2020b) software, which uses the MESA MIST stellar track models (Choi et al. 2016) to determine the best-fit stellar age, mass, radius, and density. Within this code, the Green et al. (2019) dust map was used to account for interstellar extinction, a necessary parameter for luminosity and stellar radius determination. This processing is in line with previous CKS catalogs and encapsulated 73 targets from Petigura et al. (2018), which we update with Gaia DR3 astrometry to provide the most accurate radius parameterization. Overall, these improved PM measurements yield stellar radius uncertainties of ∼2%, in agreement with other Gaia DR3–based parameterizations (Berger et al. 2023). This catalog of stellar parameters includes 239 planet-hosting targets included in the homogeneous Scaling K2 planet candidate table. We provide a list of these updated parameters in Table 3.

Appendix B
Normalization of Nonhomogeneous Samples

In order to preserve the purity of our stellar parameters, we selected stars with precise spectroscopic and astrometric parameters in Section 6. This sample selection is skewed toward bright stars for which high-resolution spectra and PM measurements are feasible to obtain. However, these cuts may not be done uniformly. For example, planet-hosting stars, known a priori, may be observed with greater frequency than a random sample would otherwise dictate. In previous work, such as Petigura et al. (2018a), these selection effects were less important since their largest contributing issue is in the total sample normalization. However, these selection effects impact the Kepler and K2 samples differently, leading to potential systematic occurrence offsets.

To first order, these sample cuts will impact the occurrence normalization. In other words, the sample reduction may reduce the number of host and nonhost systems in a nonparallel fashion, changing the extracted planet occurrence rates. To correct for this offset, we renormalized the overall occurrence to conserve the full population rates:

$$\kappa = \frac{N_{\rm Planets}}{\eta\,N_{\rm Stars}} \cdot \frac{\eta^*\,N^*_{\rm Stars}}{N^*_{\rm Planets}}. \qquad (5)$$

Here, N represents the total number of either planets within a class or stars in the sample, and η is the sample completeness. The * superscript indicates the original sample as discussed in

Table 4
Table of Occurrence Normalization Corrections (κ)

Class	Trend	Period (days)	Mission	κ
SE				
	[Fe/H]	1–10	Kepler	0.59
	[Fe/H]	1–10	K2	0.91
	[Fe/H]	10–40	Kepler	0.67
	[Fe/H]	10–40	K2	0.61
	$Z_{\rm Max}$	1–40	Kepler	1.0
	$Z_{\rm Max}$	1–40	K2	1.5
SN				
	[Fe/H]	1–10	Kepler	0.48
	[Fe/H]	1–10	K2	0.45
	[Fe/H]	10–40	Kepler	0.50
	[Fe/H]	10–40	K2	0.32
	$Z_{\rm Max}$	1–40	Kepler	1.0
	$Z_{\rm Max}$	1–40	K2	0.68
SS				
	[Fe/H]	1–10	Kepler	0.71
	[Fe/H]	1–10	K2	0.50
	[Fe/H]	10–40	Kepler	0.45
	[Fe/H]	10–40	K2	1.1
J				
	[Fe/H]	1–10	Kepler	0.48
	[Fe/H]	1–10	K2	0.66
	[Fe/H]	10–40	Kepler	0.63
	[Fe/H]	10–40	K2	1.0

Sections 2 and 3, while the lack of * indicates the reduced samples discussed in Section 6. Multiplying the appropriate occurrence correction, κ, by Equation 4 renormalizes the reduced catalog to the full sample occurrence. The respective κ values used are provided in Table 4.

This first-order correction may not be sufficient if the sample reduction artificially skews the stellar populations. Examination of the $T_{\rm eff}$ and stellar radius distributions in Figures 7 and 11 shows no significant differences with respect to the parent population (Figure 2), indicating the underlying distribution remains intact. Further evidence is in the strong alignment with the Kepler and K2 samples, which would be unlikely if significant parameter biases existed in either of the population samples.

ORCID iDs

Jon K. Zink ◉ https://orcid.org/0000-0003-1848-2063
Kevin K. Hardegree-Ullman ◉ https://orcid.org/0000-0003-3702-0382
Jessie L. Christiansen ◉ https://orcid.org/0000-0002-8035-4778
Erik A. Petigura ◉ https://orcid.org/0000-0003-0967-2893
Kiersten M. Boley ◉ https://orcid.org/0000-0001-8153-639X
Sakhee Bhure ◉ https://orcid.org/0000-0002-6673-8206
Malena Rice ◉ https://orcid.org/0000-0002-7670-670X
Samuel W. Yee ◉ https://orcid.org/0000-0001-7961-3907
Howard Isaacson ◉ https://orcid.org/0000-0002-0531-1073
Rachel B. Fernandes ◉ https://orcid.org/0000-0002-3853-7327
Andrew W. Howard ◉ https://orcid.org/0000-0001-8638-0320
Sarah Blunt ◉ https://orcid.org/0000-0002-3199-2888
Jack Lubin ◉ https://orcid.org/0000-0001-8342-7736
Ashley Chontos ◉ https://orcid.org/0000-0003-1125-2564

Daria Pidhorodetska ● https://orcid.org/0000-0001-9771-7953
Mason G. MacDougall ● https://orcid.org/0000-0003-2562-9043

References

Abdurróuf, Accetta, Aerts, K., et al. 2022, ApJS, 259, 35
Adams, E. R., Jackson, B., & Endl, M. 2016, AJ, 152, 47
Addison, B. C., Wright, D. J., Nicholson, B. A., et al. 2021, MNRAS, 502, 3704
Adibekyan, V. Z., Delgado Mena, E., Sousa, S. G., et al. 2012, A&A, 547, A36
Agati, J. L., Bonneau, D., Jorissen, A., et al. 2015, A&A, 574, A6
Andrae, R., Fouesneau, M., Sordo, R., et al. 2022, arXiv:2206.06138
Andrews, S. M., Rosenfeld, K. A., Kraus, A. L., & Wilner, D. J. 2013, ApJ, 771, 129
Baillié, K., Charnoz, S., & Pantin, E. 2016, A&A, 590, A60
Barros, S. C. C., Demangeon, O., & Deleuil, M. 2016, A&A, 594, A100
Batalha, N. M., Borucki, W. J., Koch, D. G., et al. 2010, ApJL, 713, L109
Batygin, K., Bodenheimer, P. H., & Laughlin, G. P. 2016, ApJ, 829, 114
Beaugé, C., Ferraz-Mello, S., & Michtchenko, T. A. 2012, RAA, 12, 1044
Beaugé, C., & Nesvorný, D. 2013, ApJ, 763, 12
Beleznay, M., & Kunimoto, M. 2022, MNRAS, 516, 75
Berger, T. A., Huber, D., Gaidos, E., van Saders, J. L., & Weiss, L. M. 2020a, arXiv:2005.14671
Berger, T. A., Huber, D., van Saders, J. L., et al. 2020b, AJ, 159, 280
Berger, T. A., Schlieder, J. E., & Huber, D. 2023, arXiv:2301.11338
Bergsten, G. J., Pascucci, I., Mulders, G. D., Fernandes, R. B., & Koskinen, T. T. 2022, AJ, 164, 190
Biersteker, J. B., & Schlichting, H. E. 2019, MNRAS, 485, 4454
Boley, A. C., Granados Contreras, A. P., & Gladman, B. 2016, ApJL, 817, L17
Boley, A. C., Morris, M. A., & Ford, E. B. 2014, ApJL, 792, L27
Boley, K. M., Wang, J., Zinn, J. C., et al. 2021, AJ, 162, 85
Borucki, W. J., Koch, D. G., Basri, G., et al. 2011, ApJ, 736, 19
Bovy, J. 2015, ApJS, 216, 29
Brady, M. T., Petigura, E. A., Knutson, H. A., et al. 2018, AJ, 156, 147
Brewer, J. M., Wang, S., Fischer, D. A., & Foreman-Mackey, D. 2018, ApJL, 867, L3
Buchhave, L. A., Latham, D. W., Johansen, A., et al. 2012, Natur, 486, 375
Buck, T., Obreja, A., Macciò, A. V., et al. 2020, MNRAS, 491, 3461
Burke, C. J. 2008, ApJ, 679, 1566
Burke, C. J., Christiansen, J. L., Mullally, F., et al. 2015, ApJ, 809, 8
Chen, D.-C., Yang, J.-Y., Xie, J.-W., et al. 2021, AJ, 162, 100
Cheng, J. Y., Rockosi, C. M., Morrison, H. L., et al. 2012, ApJ, 746, 149
Choi, J., Dotter, A., Conroy, C., et al. 2016, ApJ, 823, 102
Christiansen, J. L. 2017, Technial Report, KSCI-19110-001 Kepler Science Document
Christiansen, J. L., Bhure, S., Zink, J. K., et al. 2022, AJ, 163, 244
Christiansen, J. L., Clarke, B. D., Burke, C. J., et al. 2015, ApJ, 810, 95
Christiansen, J. L., Clarke, B. D., Burke, C. J., et al. 2020, arXiv:2010.04796
Christiansen, J. L., Jenkins, J. M., Caldwell, D. A., et al. 2012, PASP, 124, 1279
Coughlin, J. L. 2017, Technical Report, KSCI-19114-002Kepler Science Document
Creevey, O. L., Sordo, R., Pailler, F., et al. 2022, arXiv:2206.05864
Crossfield, I. J. M., Ciardi, D. R., Petigura, E. A., et al. 2016, ApJS, 226, 7
Csizmadia, S., Hatzes, A., Gandolfi, D., et al. 2015, A&A, 584, A13
Dawson, R. I., & Johnson, J. A. 2018, ARA&A, 56, 175
Dawson, R. I., & Murray-Clay, R. A. 2013, ApJL, 767, L24
Dressing, C. D., & Charbonneau, D. 2013, ApJ, 767, 95
Dressing, C. D., & Charbonneau, D. 2015, ApJ, 807, 45
Dressing, C. D., Vanderburg, A., Schlieder, J. E., et al. 2017, AJ, 154, 207
Fabrycky, D., & Tremaine, S. 2007, ApJ, 669, 1298
Fischer, D. A., & Valenti, J. 2005, ApJ, 622, 1102
Foreman-Mackey, D., Hogg, D. W., & Morton, T. D. 2014, ApJ, 795, 64
Fouesneau, M., Frémat, Y., Andrae, R., et al. 2022, arXiv:2206.05992
Fressin, F., Torres, G., Charbonneau, D., et al. 2013, ApJ, 766, 81
Fulton, B. J., Petigura, E. A., Howard, A. W., et al. 2017, AJ, 154, 109
Gaia Collaboration, A., Vallenari, A., Brown, A. G. A., et al. 2022, arXiv:2208.00211
Ghezzi, L., Cunha, K., Smith, V. V., et al. 2010, ApJ, 720, 1290
Goldberg, M., Batygin, K., & Morbidelli, A. 2022, Icar, 388, 115206
Goldreich, P., & Tremaine, S. 1980, ApJ, 241, 425
Gonzalez, G. 2009, MNRAS, 399, L103

Green, G. M., Schlafly, E., Zucker, C., Speagle, J. S., & Finkbeiner, D. 2019, ApJ, 887, 93
Guo, X., Johnson, J. A., Mann, A. W., et al. 2017, ApJ, 838, 25
Gupta, A., & Schlichting, H. E. 2019, MNRAS, 487, 24
Hallatt, T., & Lee, E. J. 2022, ApJ, 924, 9
Hardegree-Ullman, K. K., Cushing, M. C., Muirhead, P. S., & Christiansen, J. L. 2019, AJ, 158, 75
Hardegree-Ullman, K. K., Zink, J. K., Christiansen, J. L., et al. 2020, ApJS, 247, 28
Harris, W. E. 1976, AJ, 81, 1095
He, M. Y., Ford, E. B., & Ragozzine, D. 2019, MNRAS, 490, 4575
Ho, C. S. K., & Van Eylen, V. 2023, MNRAS, 519, 4056
Howard, A. W., Johnson, J. A., Marcy, G. W., et al. 2010, ApJ, 721, 1467
Howard, A. W., Marcy, G. W., Bryson, S. T., et al. 2012, ApJS, 201, 15
Howell, S. B., Sobeck, C., Haas, M., et al. 2014, PASP, 126, 398
Hsu, D. C., Ford, E. B., Ragozzine, D., & Ashby, K. 2019, AJ, 158, 109
Huber, D., Bryson, S. T., Haas, M. R., et al. 2016, ApJS, 224, 2
Huber, D., Zinn, J., Bojsen-Hansen, M., et al. 2017, ApJ, 844, 102
Ionov, D. E., Pavlyuchenkov, Y. N., & Shematovich, V. I. 2018, MNRAS, 476, 5639
Jenkins, J. M., Caldwell, D. A., Chandrasekaran, H., et al. 2010, ApJL, 713, L87
Johnson, J. A., Aller, K. M., Howard, A. W., & Crepp, J. R. 2010, PASP, 122, 905
Johnson, J. A., Butler, R. P., Marcy, G. W., et al. 2007, ApJ, 670, 833
Katz, D., Sartoretti, P., Guerrier, A., et al. 2022, arXiv:2206.05902
Koch, D. G., Borucki, W. J., Rowe, J. F., et al. 2010, ApJ, 713, L131
Kolecki, J. R., Wang, J., Johnson, J. A., et al. 2021, AJ, 162, 125
Kruse, E., Agol, E., Luger, R., & Foreman-Mackey, D. 2019, ApJS, 244, 11
Kuiper, G. P. 1938, ApJ, 88, 472
Lee, E. J., & Chiang, E. 2017, ApJ, 842, 40
Lee, E. J., & Connors, N. J. 2021, ApJ, 908, 32
Lin, D. N. C., Bodenheimer, P., & Richardson, D. C. 1996, Natur, 380, 606
Lindegren, L., Hernández, J., Bombrun, A., et al. 2018, A&A, 616, A2
Livingston, J. H., Endl, M., Dai, F., et al. 2018, AJ, 156, 78
Lodders, K. 2003, ApJ, 591, 1220
Lopez, E. D., & Fortney, J. J. 2013, ApJ, 776, 2
Lopez, E. D., & Rice, K. 2018, MNRAS, 479, 5303
Luger, R., Agol, E., Kruse, E., et al. 2016, AJ, 152, 100
Luger, R., Kruse, E., Foreman-Mackey, D., Agol, E., & Saunders, N. 2018, AJ, 156, 99
Mayo, A. W., Vanderburg, A., Latham, D. W., et al. 2018, AJ, 155, 136
Mazeh, T., Holczer, T., & Faigler, S. 2016, A&A, 589, A75
McTier, M. A. S., & Kipping, D. M. 2019, MNRAS, 489, 2505
Millholland, S., Petigura, E., & Batygin, K. 2020, ApJ, 897, 7
Muirhead, P. S., Mann, A. W., Vanderburg, A., et al. 2015, ApJ, 801, 18
Mulders, G. D., Drążkowska, J., van der Marel, N., Ciesla, F. J., & Pascucci, I. 2021, ApJL, 920, L1
Mulders, G. D., Pascucci, I., & Apai, D. 2015, ApJ, 798, 112
Mulders, G. D., Pascucci, I., Apai, D., & Ciesla, F. J. 2018, AJ, 156, 24
Mullally, F., Coughlin, J. L., Thompson, S. E., et al. 2015, ApJS, 217, 31
Nagasawa, M., Ida, S., & Bessho, T. 2008, ApJ, 678, 498
NASA Exoplanet Archive 2023, Kepler Objects of Interest Cumulative Table, Version: 2023-02-09 08:00, NExScI-Caltech/IPAC, doi:10.26133/NEA4
Neil, A. R., & Rogers, L. A. 2020, ApJ, 891, 12
Niu, Z., Yuan, H., Wang, S., & Liu, J. 2021, ApJ, 922, 211
Nowak, G., Palle, E., Gandolfi, D., et al. 2020, MNRAS, 497, 4423
Owen, J. E., & Lai, D. 2018, MNRAS, 479, 5012
Owen, J. E., & Wu, Y. 2017, ApJ, 847, 29
Park, M. J., Yi, S. K., Peirani, S., et al. 2021, ApJS, 254, 2
Petigura, E. 2015, arXiv:1510.03902
Petigura, E. A., Crossfield, I. J. M., Isaacson, H., et al. 2018b, AJ, 155, 21
Petigura, E. A., Howard, A. W., & Marcy, G. W. 2013a, PNAS, 110, 19273
Petigura, E. A., Howard, A. W., Marcy, G. W., et al. 2017a, AJ, 154, 107
Petigura, E. A., Livingston, J., Batygin, K., et al. 2020, AJ, 159, 2
Petigura, E. A., Marcy, G. W., & Howard, A. W. 2013b, ApJ, 770, 69
Petigura, E. A., Marcy, G. W., Winn, J. N., et al. 2018a, AJ, 155, 89
Petigura, E. A., Rogers, J. G., Isaacson, H., et al. 2022, AJ, 163, 179
Petigura, E. A., Sinukoff, E., Lopez, E. D., et al. 2017b, AJ, 153, 142
Petrovich, C., & Tremaine, S. 2016, ApJ, 829, 132
Petrovich, C., Tremaine, S., & Rafikov, R. 2014, ApJ, 786, 101
Pollack, J. B., Hubickyj, O., Bodenheimer, P., et al. 1996, Icar, 124, 62
Pope, B. J. S., Parviainen, H., & Aigrain, S. 2016, MNRAS, 461, 3399
Price-Whelan, A. M. 2017, JOSS, 2, 388
Qian, Y., & Wu, Y. 2021, AJ, 161, 201
Rasio, F. A., & Ford, E. B. 1996, Sci, 274, 954
Rauer, H., Catala, C., Aerts, C., et al. 2014, ExA, 38, 249

Rice, M., Wang, S., Wang, X.-Y., et al. 2022, AJ, 164, 104
Ricker, G. R., Winn, J. N., Vanderspek, R., et al. 2015, JATIS, 1, 014003
Rix, H.-W., & Bovy, J. 2013, A&ARv, 21, 61
Rogers, J. G., & Owen, J. E. 2021, MNRAS, 503, 1526
Rogers, J. G., Schlichting, H. E., & Owen, J. E. 2023, ApJL, 947, L19
Santerne, A., Moutou, C., Tsantaki, M., et al. 2016, A&A, 587, A64
Shabram, M., Demory, B.-O., Cisewski, J., Ford, E. B., & Rogers, L. 2016, ApJ, 820, 93
Sousa, S. G., Santos, N. C., Mayor, M., et al. 2008, A&A, 487, 373
Schlesinger, Katharine J., Johnson, Jennifer A., Rockosi, Constance M., et al. 2014, ApJ, 791, 112
Spalding, C., & Batygin, K. 2014, ApJ, 790, 42
Tanaka, K. E. I., & Omukai, K. 2014, MNRAS, 439, 1884
Thompson, S. E., Coughlin, J. L., Hoffman, K., et al. 2018, ApJS, 235, 38
Udry, S., Mayor, M., & Santos, N. C. 2003, A&A, 407, 369
Van Cleve, J. E., Howell, S. B., Smith, J. C., et al. 2016, PASP, 128, 075002
Van Eylen, V., Agentoft, C., Lundkvist, M. S., et al. 2018, MNRAS, 479, 4786
Vanderburg, A., Latham, D. W., Buchhave, L. A., et al. 2016, ApJS, 222, 14
Venn, K. A., Irwin, M., Shetrone, M. D., et al. 2004, AJ, 128, 1177

Vogt, S. S., Allen, S. L., Bigelow, B. C., et al. 1994, Proc. SPIE, 2198, 362
Wallerstein, G. 1962, ApJS, 6, 407
Wang, C., Huang, Y., Yuan, H., et al. 2022, ApJS, 259, 51
Wilson, R. F., Cañas, C. I., Majewski, S. R., et al. 2022, AJ, 163, 128
Wittenmyer, R. A., O'Toole, S. J., Jones, H. R. A., et al. 2010, ApJ, 722, 1854
Wu, Y., & Lithwick, Y. 2011, ApJ, 735, 109
Wu, Y., & Murray, N. 2003, ApJ, 589, 605
Yee, S. W., Petigura, E. A., & von Braun, K. 2017, ApJ, 836, 77
Youdin, A. N. 2011, ApJ, 742, 38
Yu, L., Crossfield, I. J. M., Schlieder, J. E., et al. 2018, AJ, 156, 22
Zink, J. K., Christiansen, J. L., & Hansen, B. M. S. 2019a, MNRAS, 483, 4479
Zink, J. K., Hardegree-Ullman, K. K., Christiansen, J. L., et al. 2020a, AJ, 159, 154
Zink, J. K., Hardegree-Ullman, K. K., Christiansen, J. L., et al. 2020b, AJ, 160, 94
Zink, J. K., Hardegree-Ullman, K. K., Christiansen, J. L., et al. 2019b, RNAAS, 3, 43
Zink, J. K., Hardegree-Ullman, K. K., Christiansen, J. L., et al. 2021, AJ, 162, 259